General Disclaimer

One or more of the Following Statements may affect this Document

- This document has been reproduced from the best copy furnished by the organizational source. It is being released in the interest of making available as much information as possible.

- This document may contain data, which exceeds the sheet parameters. It was furnished in this condition by the organizational source and is the best copy available.

- This document may contain tone-on-tone or color graphs, charts and/or pictures, which have been reproduced in black and white.

- This document is paginated as submitted by the original source.

- Portions of this document are not fully legible due to the historical nature of some of the material. However, it is the best reproduction available from the original submission.

Produced by the NASA Center for Aerospace Information (CASI)

N77
25048

UNCLAS

UAH Research Report No. 200

The University of Alabama in Huntsville
School of Science and Engineering
P. O. Box 1247
Huntsville, Alabama 35807

THE SPECIFIC LIGHT OUTPUT OF CESIUM IODIDE CRYSTALS

Final Technical Report
Contract NAS8-24953
(6-26-69/12-31-76)

(NASA-CR-150267) THE SPECIFIC LIGHT OUTPUT OF CESIUM IODIDE CRYSTALS Final Technical Report, 26 Jun. 1969 - 31 Dec. 1976 (Alabama Univ., Huntsville.) 82 p HC A05/MF A01 CSCL 03B G3/93

N77-25047
THRU
N77-25050
Unclas
29081

By

John C. Gregory
Principal Investigator

Prepared for

George C. Marshall Space Flight Center
National Aeronautics and Space Administration
Marshall Space Flight Center, Alabama 35812

UAH Research Report No. 200

The University of Alabama in Huntsville
School of Science and Engineering
P. O. Box 1247
Huntsville, Alabama 35807

THE SPECIFIC LIGHT OUTPUT OF CESIUM IODIDE CRYSTALS

Final Technical Report
Contract NAS8-24953
(6-26-69/12-31-76)

By

John C. Gregory
Principal Investigator

Prepared for

George C. Marshall Space Flight Center
National Aeronautics and Space Administration
Marshall Space Flight Center, Alabama 35812

TABLE OF CONTENTS

1. Large Area Ion Chambers for a High Energy Cosmic Ray Experiment 1

2. Scintillating Plastic Fibers as Light Pipes for a Cosmic Ray Hodoscope 45

3. Evaluation of Clad Scintillating Light Pipes 59

4. Location of Transient Gamma-Ray Sources with Thin Flat Scintillators 64

5. An X-ray Shadowgraph to Locate Transient High-Energy Celestial Sources 70

N77-25048

INTRODUCTION

Ion chambers are a prime choice for selection as a dE/dx detector for cosmic ray charge identification. They exhibit good resolution and linearity over a wide energy deposition range without interposing much mass in the particle beam, and have reasonably uniform response over large detector areas.

The pulse ion chambers described in this report originally formed part of the High Energy Cosmic Ray Experiment for the high energy astronomical observatory (HEAO), (Ormes et. al., 1970), and also part of the Marshall Space Flight Center - UAH cosmic ray experiment. The objective of the balloon flight program is to perform high resolution measurement of the iron group nuclei with the intention of determining individual abundances in the cosmic ray flux at the earth of particles with z = 22 to 30. The experience being gained with these types of detector system is allowing a study of the feasibility of building much larger area detectors to extend the charge resolution measurements to higher z and energy.

The balloon flight system which has now flown successfully a total of three times is shown in Figure 1. Of the three types of dE/dx detectors used in the experiment, pulse ion chambers, Cerenkov radiators and scintillators, the first has the best z resolution over a wide range of particle z and energy. The plastic scintillators define the particle acceptance cone of the telescope while the Cerenkov detector aids in rejection of low energy particle background and measurement of particle velocity.

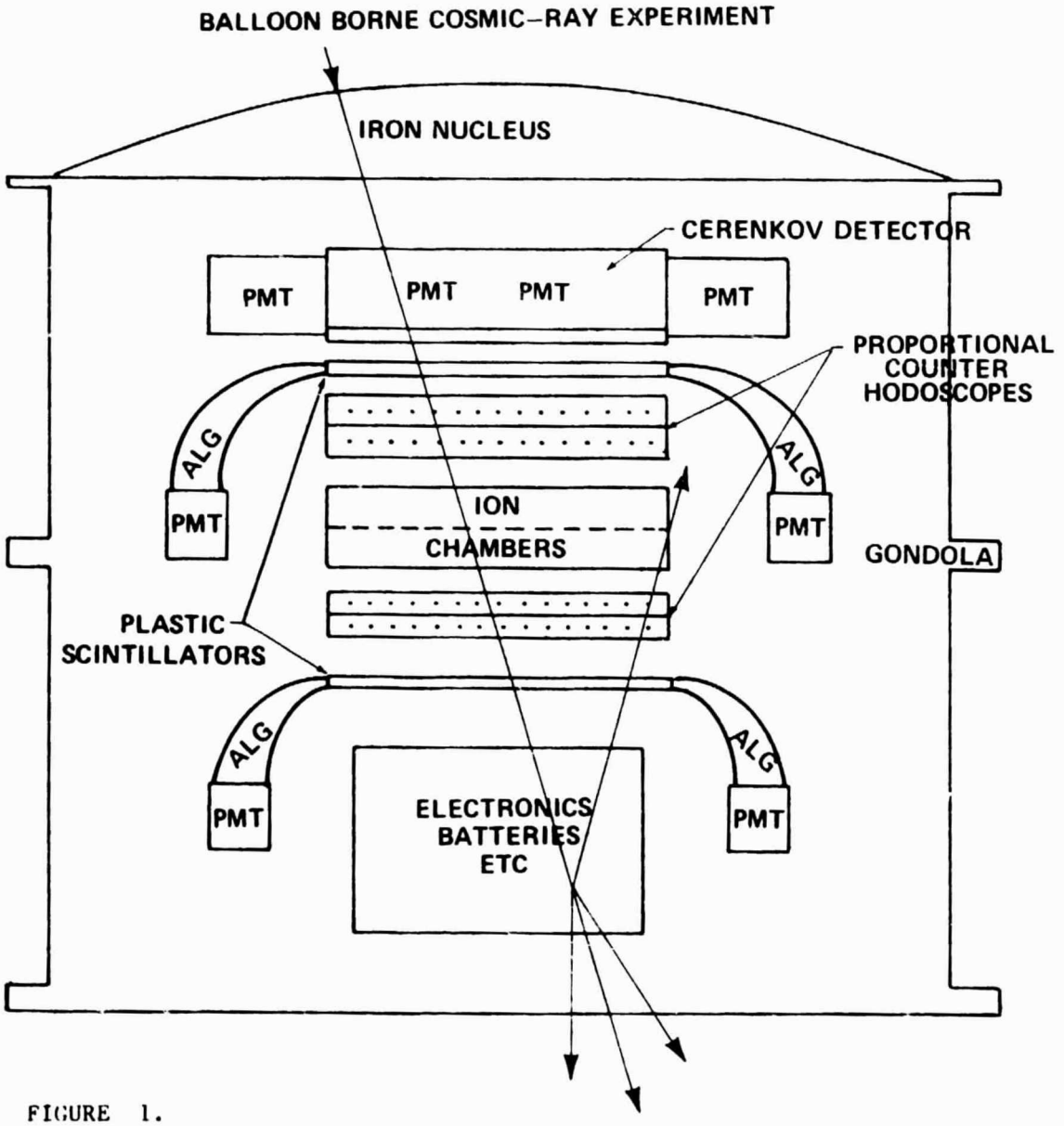
BALLOON BORNE COSMIC–RAY EXPERIMENT
IRON NUCLEUS
CERENKOV DETECTOR
PMT
PMT
PMT
PMT
PROPORTIONAL
COUNTER
HODOSCOPES
ALG
ALG
PMT
ION
CHAMBERS
PMT
GONDOLA
PLASTIC
SCINTILLATORS
ALG
ALG
PMT
ELECTRONICS
BATTERIES
ETC
PMT

FIGURE 1.

This report includes work performed by the MSFC-UAH cosmic ray group as a whole. T. A. Parnell (MSFC) has been intimately involved in the project from the outset; G. A. Guenther and U. Pollvogt, formerly with the UAH, were involved in the early stages of design; J. Derrickson (MSFC) performed some of the gas-studies; and T. A. Rygg, NAS Research Associate, computed the estimated integrated particle distributions for the balloon flight system.

THEORETICAL APPROACH

When 'protonlike' particles pass through matter they lose energy by ionization and excitation of absorber atoms, Cerenkov radiative loss, bremsstrahlung, and nuclear interactions. The electromagnetic radiation losses are negligible compared to the ionization and excitation energy losses. Nuclear interactions are rendered very improbable by the low mass thickness of the detectors; a particle event being rejected if such an interaction occurs.

For charged particles with rest mass much greater than that of the electron, the energy loss by ionization in an absorbing medium is given by the theoretical expression attributed to Bethe and Bloch (e.g. see Livingston and Bethe, 1937):

$$-\frac{dE}{dx} = 4\pi r_o^2 \quad \frac{\rho L Z}{A} \cdot \frac{mc^2 z^2}{\beta} \quad \left[\ell n \frac{2mc^2\beta^2}{ZI(1-\beta^2)} - \beta^2 \right] \text{ MeV cm}^{-1}$$

where mc^2 = rest energy of electron (=.51 MeV)

r_o^2 = classical electron radius, e^2/mc^2

L = Avogadro's number

ρ, Z, and A are the density, atomic number and atomic weight of the absorber

z = atomic number of incident particle

β = v/c where v is the velocity of the particle

I = average excitation potential per electron and may be taken as 11.5×10^{-6} MeV.

In a thin absorber β and and $^{dE}/_{dx}$ are assumed constant and the energy

loss given by the Bethe formula is proportional to the path length in the detector x $\rho \frac{Z}{A}$. For ideal gases ρ/A is constant so that calculated energy losses in different gas fillings for the same particle charge and energy are directly proportional to the ratio of Z's for the two gases. The specific energy loss is also seen from the Bethe formula to depend on the particle parameters z^2 and β. For balloon flights from Palestine, Texas the relativistic rise in dE/dx for particles with energies between the geomagnetic cutoff energy and 10 GeV or so is about 25-30%. In this energy internal the flux falls off by a factor of 30 approximately.

For thin detectors the energy loss by a beam of monoenergetic particles is subject to rather wide fluctuations. These fluctuations, called straggling. are caused by statistical variations in the finite number of events which occur in the energy loss process. As a result, the energy loss distribution for monoenergetic fast charged particles is quite wide and skewed to the high energy side since the number of large energy loss events is small. Theoretical treatment of energy loss straggling in thin absorbers was first made by Landau (1944). The problem was further analyzed by Symon (1949) and Vavilov (1957).

Gas-filled ionization chambers and other thin detectors exhibit energy distributions considerably narrower than that predicted from Vavilov distributions. It must be emphasised that these detectors measure energy deposit within the detector volume rather than energy lost by the particle in the same volume. Watts (1972) has calculated energy deposit distribution functions for particles with several values of z up to 26 (iron) in gas-filled ionization chambers. His calculations treated the transport of energy by δ-rays (fast electrons produced by high energy transfer events between the relativistic particle and absorber electrons) from the point of primary

energy loss by the particle and along the δ-ray track. Both energy transported out of the detector volume and energy transported into the detector from prior energy loss events in the counter diaphragm were considered. The energy deposit distribution is consequently a very complex function of detector composition and geometry and does not lend itself to easy relative calculation say for a change of gas or counter thickness.

An important result of this work was the quantified explanation of energy deposit distributions narrower than the Vavilov energy loss distributions. The variation of distribution maximum goes as z^2 in accordance with Bethe, while the variation of distribution width has an approximate z dependence.

Since high energy δ-rays produced above the detector volume deposit more energy in the counter than high energy δ-rays produced in the volume, reductions in the mass above the ionization chambers should result in a reduction of the width of the energy deposit distribution.

Energy deposit distributions for particles of 10 GeV per nucleon and charges around z = 26 normally incident upon an ion chamber were calculated by Watts for our geometries and with argon and xenon gas fills. These curves have been replotted using cosmic ray abundances given by Juliusson, Meyer and Mueller (1972) and are shown in figures 2, 3 and 4. Numbers for particles of each z are given for a balloon flight of 10 hours duration at Palestine, Texas.

Because of increased energy deposit in xenon compared with argon, the resolution of the iron peak is better with xenon for the same thickness. The improvement is not simply in the square root of the ratio of their atomic numbers, since the δ-rays effects negate some of the resolution increase.

FIGURE 2.

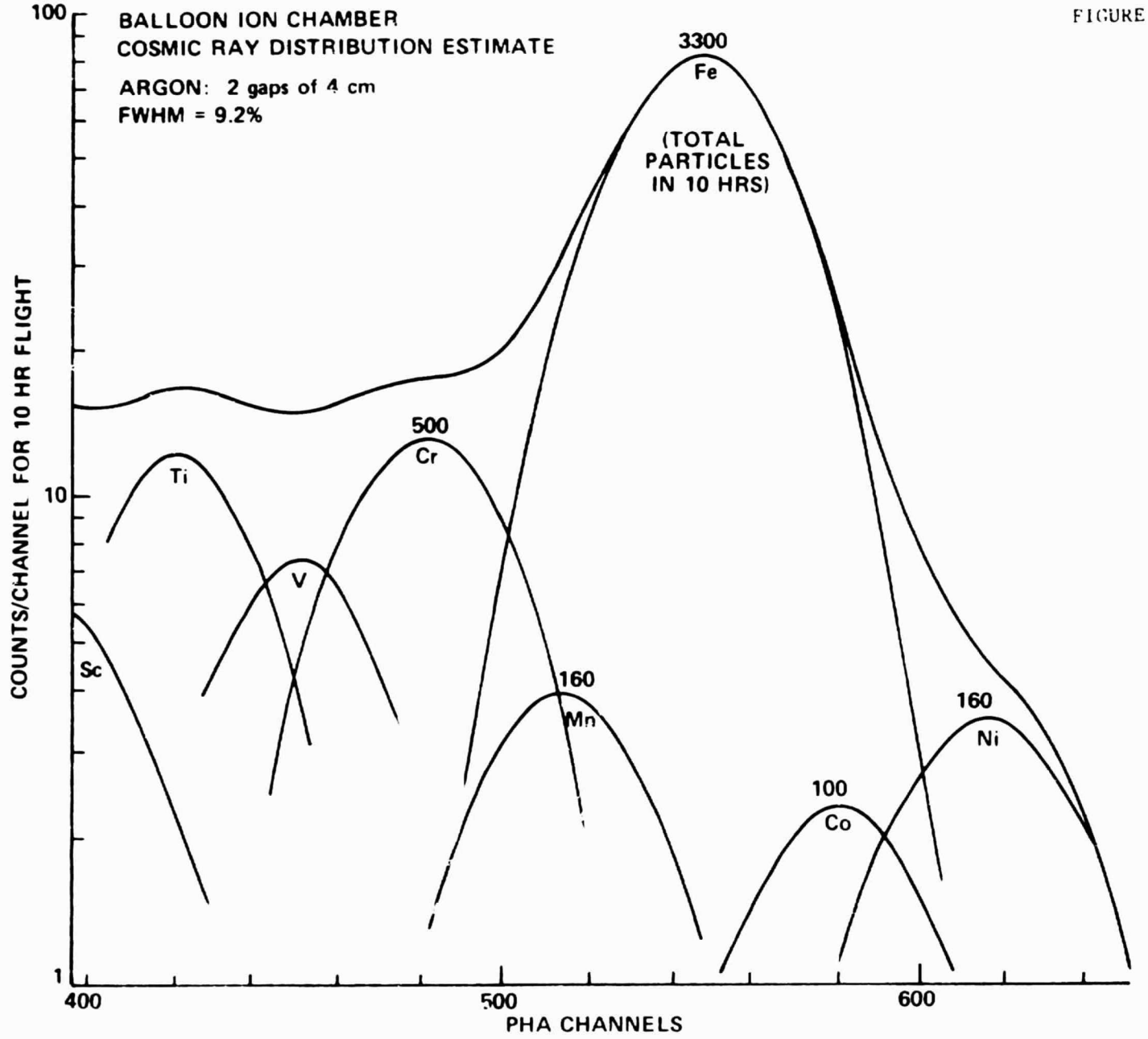
BALLOON ION CHAMBER
COSMIC RAY DISTRIBUTION ESTIMATE
ARGON: 2 gaps of 4 cm
FWHM = 9.2%
3300
Fe
(TOTAL PARTICLES IN 10 HRS)
500
Cr
Ti
V
Sc
160
Mn
100
Co
160
Ni
100
10
1
COUNTS/CHANNEL FOR 10 HR FLIGHT
400
500
600
PHA CHANNELS

FIGURE 3.

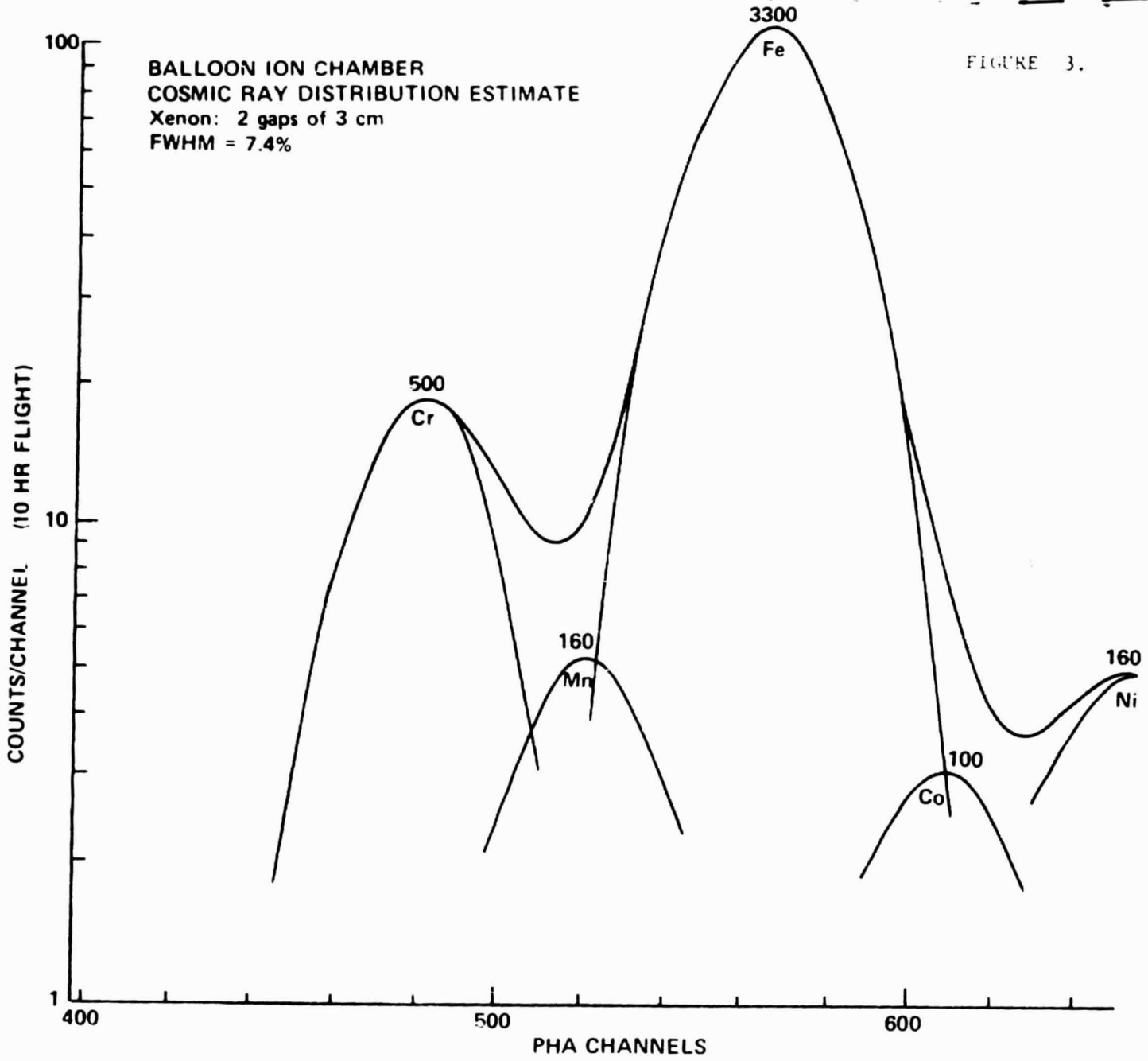
BALLOON ION CHAMBER
COSMIC RAY DISTRIBUTION ESTIMATE
Xenon: 2 gaps of 3 cm
FWHM = 7.4%
COUNTS/CHANNEL (10 HR FLIGHT)
100
10
1
400
500
600
PHA CHANNELS
3300
Fe
500
Cr
160
Mn
100
Co
160
Ni

FIGURE 4.

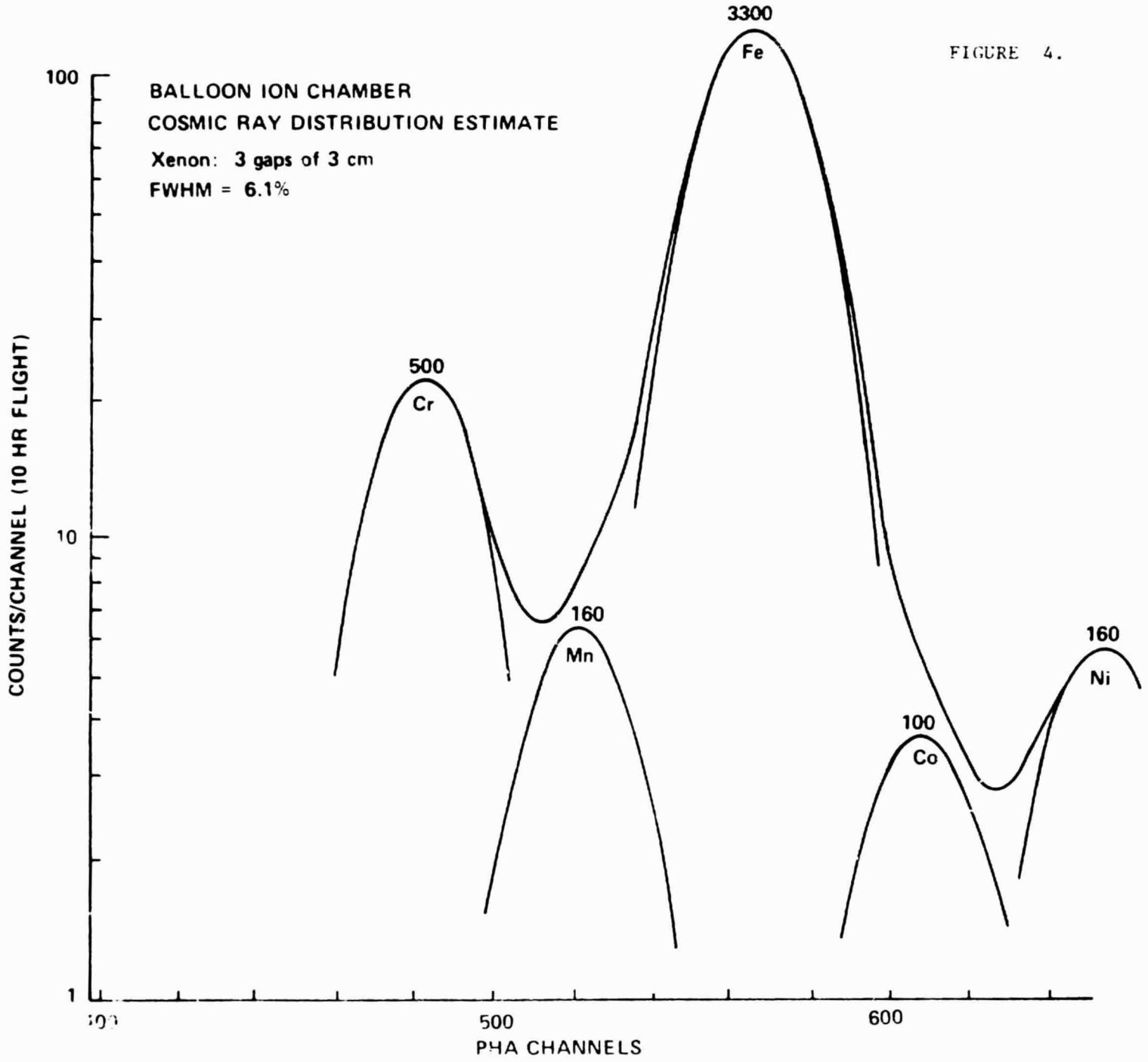
BALLOON ION CHAMBER
COSMIC RAY DISTRIBUTION ESTIMATE
Xenon: 3 gaps of 3 cm
FWHM = 6.1%
COUNTS/CHANNEL (10 HR FLIGHT)
100
10
1
3300
Fe
500
Cr
160
Mn
100
Co
160
Ni
500
600
PHA CHANNELS

A calculation was not made for our specific geometry of 2 gaps of 8.4 cm. of xenon each, but an inexact estimate yields a resolution of better than 5 per cent FWHM for a monoenergetic iron beam at several GeV per nucleon.

Superimposed on the energy deposition frequency distribution are further uncertainties the most important of which are: 1) angular uncertainty of the particle track defined by the proportional counter hodoscope, 2) relativistic rise of energy deposit with particle energy 3) charge collection efficiency within the ion chamber as a function of position, counter lifetime etc., and 4) amplifier noise. These effects, with the exception of 2), are discussed in the next section.

LABORATORY DESIGN STUDIES

Mechanical Construction

Each of the two ion chambers is comprised of 3 stainless steel mesh planes, the outer two electrically insulated from the middle, and all three from the housing. The square housings of internal dimension 67.4 cm are of aluminum (chosen for its low density) 0.125 in thick; one chamber being welded out of plate and the other machined from a single piece. One housing received a chromate conversion coating and the other was anodized. Since surface finish is of great significance in the lifetime expectancy of gas-filled detectors, it was hoped to make a comparison. However, for both balloon flights we have operated the two housings bolted together with a common Xe-7% CH_4 fill. Further details of the housing preparation and vacuum integrity testing are included in appendix A.

Three photographs of the electrode structure and housing are shown in Figures 5, 6 and 7. Figure 5 shows an electrode assembly prior to installation in a housing, Figure 6 a closeup of the electrode frames in the vicinity of the feedthroughs, and Figure 7 an overall view. The dark spot in the center of the top cathode is an Am-241 source.

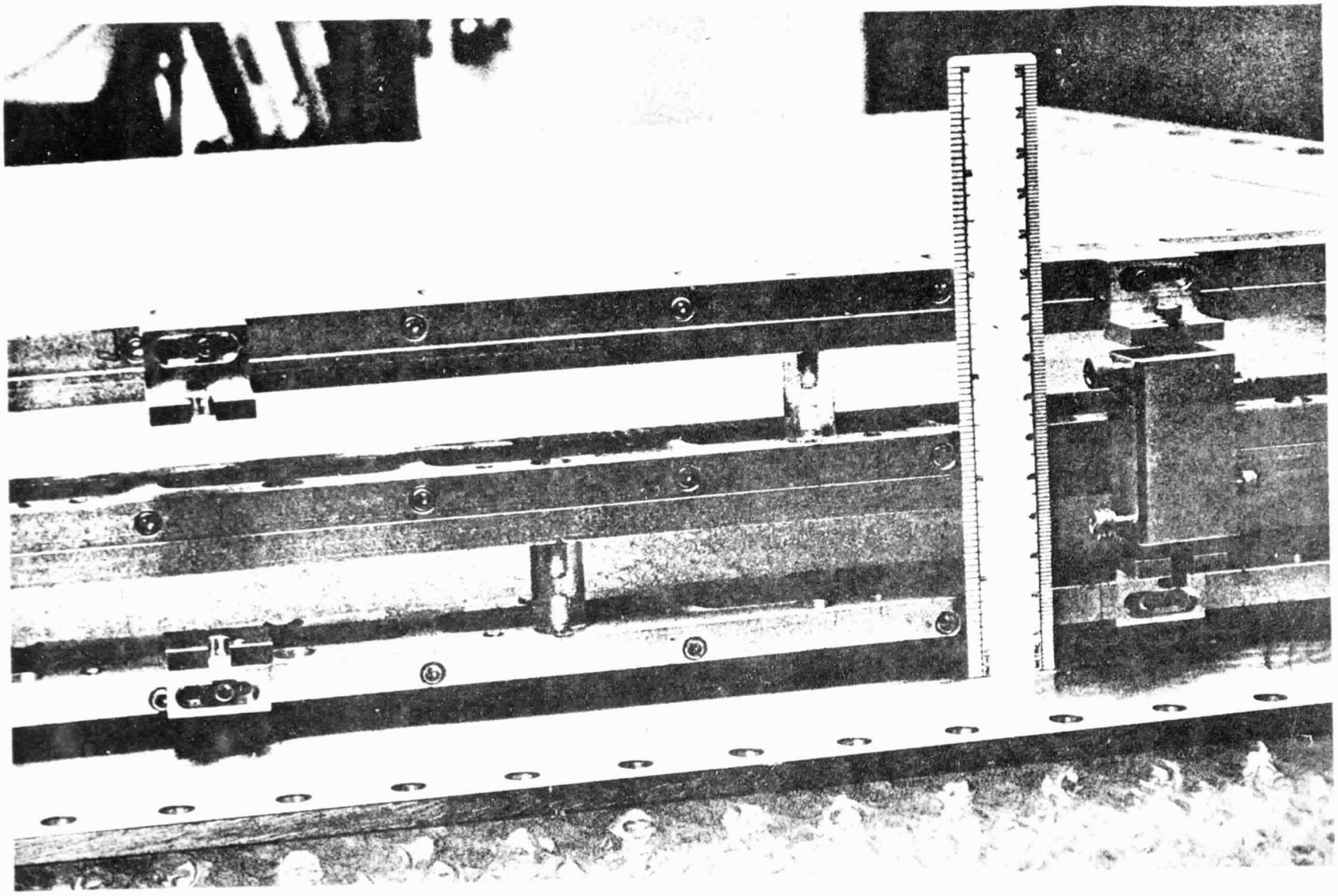

FIGURE 5.

REPRODUCIBILITY OF THE
ORIGINAL PAGE IS POOR

REPRODUCIBILITY OF THE
ORIGINAL PAGE IS POOR

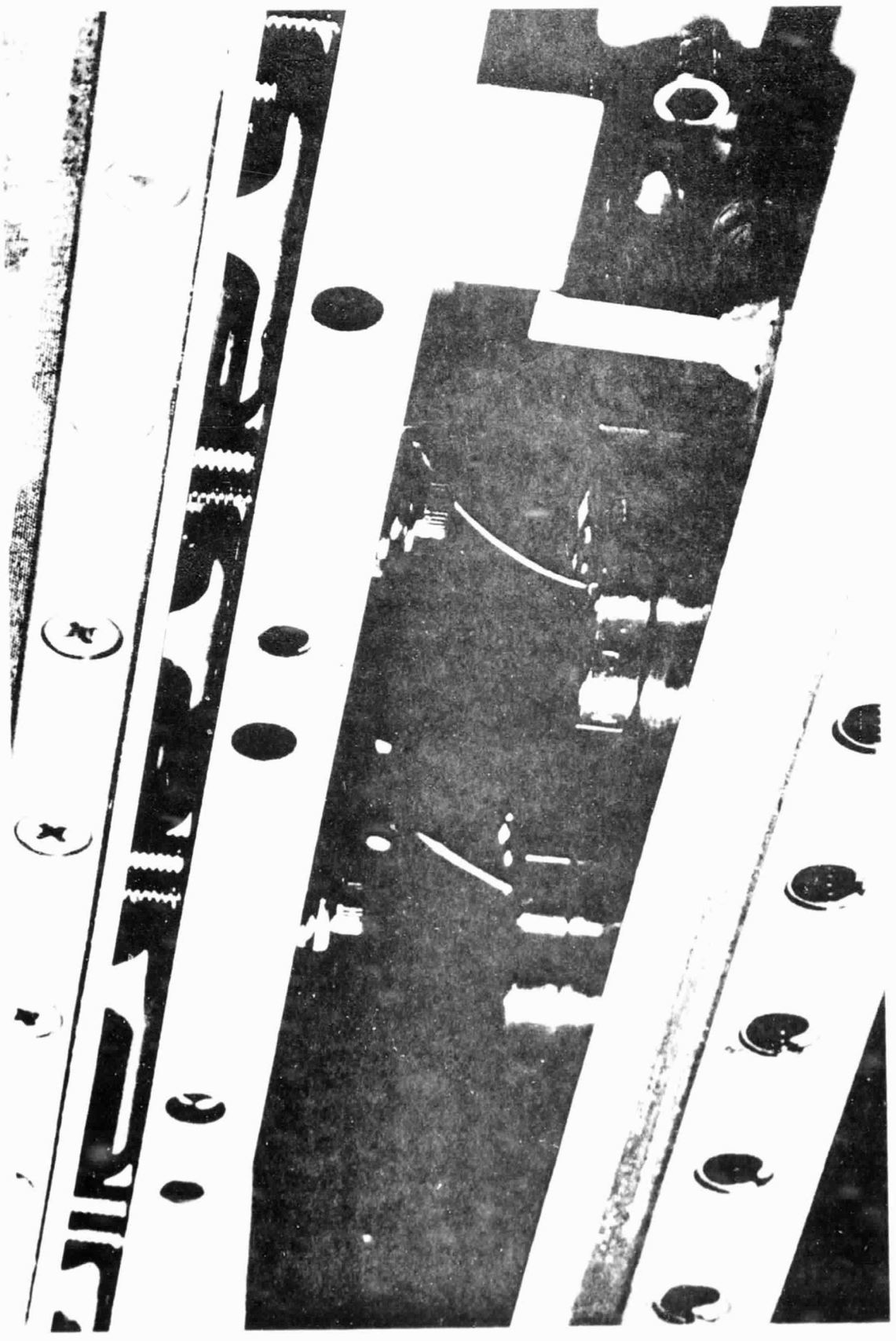

FIGURE 6.

REPRODUCIBILITY OF THE
ORIGINAL PAGE IS POOR

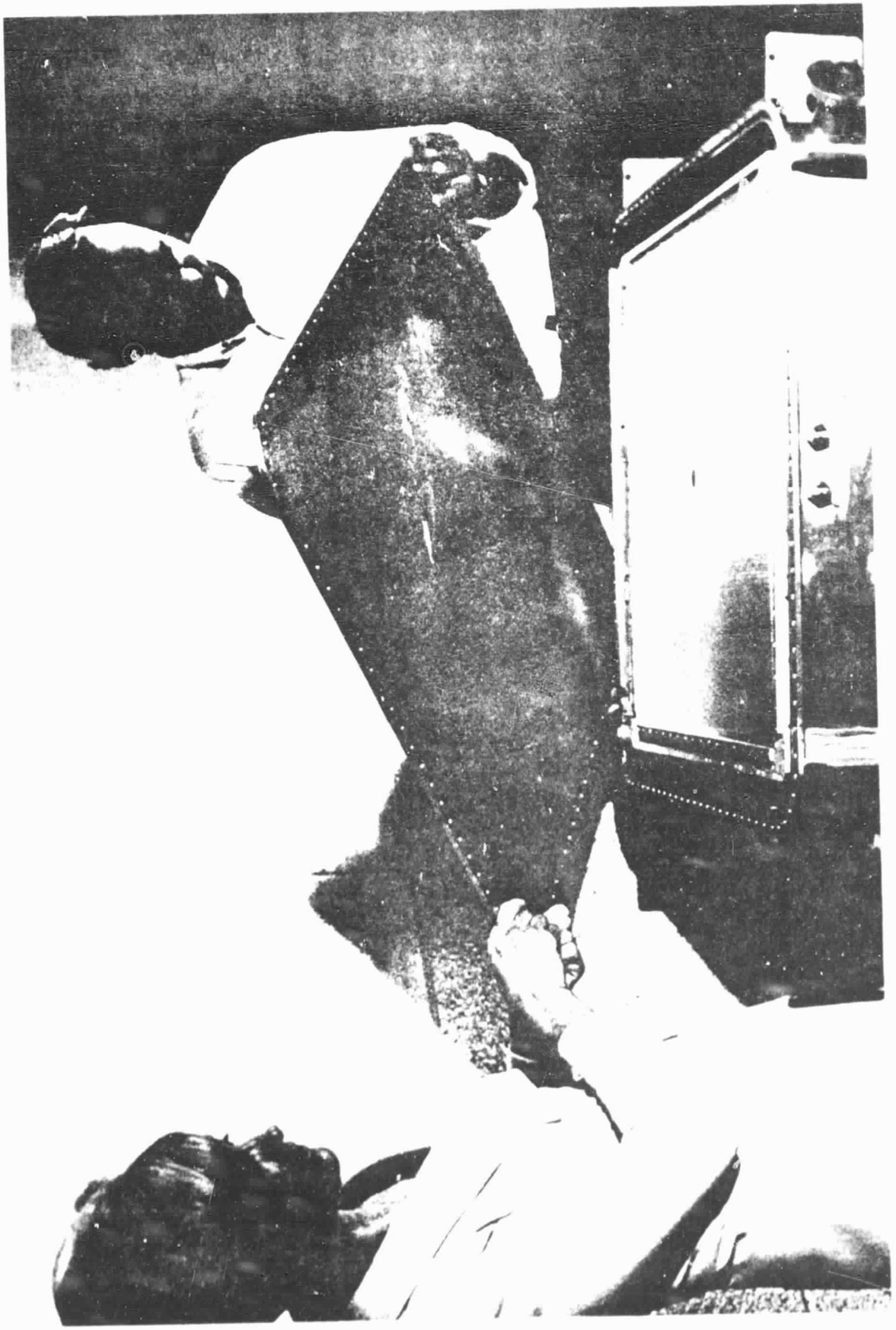

Each mesh plane is tightly stretched over square aluminum frames, 62 cm outside dimension and 52 cm inside. Two frames with a total thickness of 2 cm hold each plane rigidly, some metal being removed to reduce weight. The mesh screens are of 0.003 in (76 micrometer) stainless steel wire, 100 wires in^{-1}. (40 mm^{-1}) with an optical transparency of 50%.

Spacing is maintained between anode and cathodes, and between plane assembly and the housing, with ceramic and plexiglas insulators. Organic contamination is not considered a problem in ion chambers (unlike proportional counters). The diaphragms are 0.25 in thick aluminum honeycomb with a solid frame and 0.020 in aluminum faceplates. The diaphragms are sealed to the housing with Viton "O" rings.

There are two insulated feedthroughs for the anode and cathodes and one 1.5 in port to which is attached a Viton-seated high vacuum valve which remains with the counter after gas fill.

A stainless steel foil 0.002 in thickness is placed between the two ion chambers to render the outputs independent of each other.

Field Uniformity Checks

The gap width of ion chamber 1 after final assembly for a balloon flight was checked. Measured deviation from the nominal 4.2 cm (1.654 in) nowhere exceeded ± .010 in or ± 0.6%. At the normal operating voltage of 1000 V this produces an electric field variation of ± 6 V ; and since the measured charge collection efficiency has a slope of only 0.85% per 100 V at this operating voltage, variation of charge collection efficiency due to mechanical variation in gap width is seen to be negligible, (± 0.05%).

Field uniformity at the edges of the ion chamber grids was investigated by field-plotting. The electrode structure was painted at a scale of 2:1 on

FIGURE 8.

ISO POTENTIALS FOR THE BALLOON ION CHAMBER

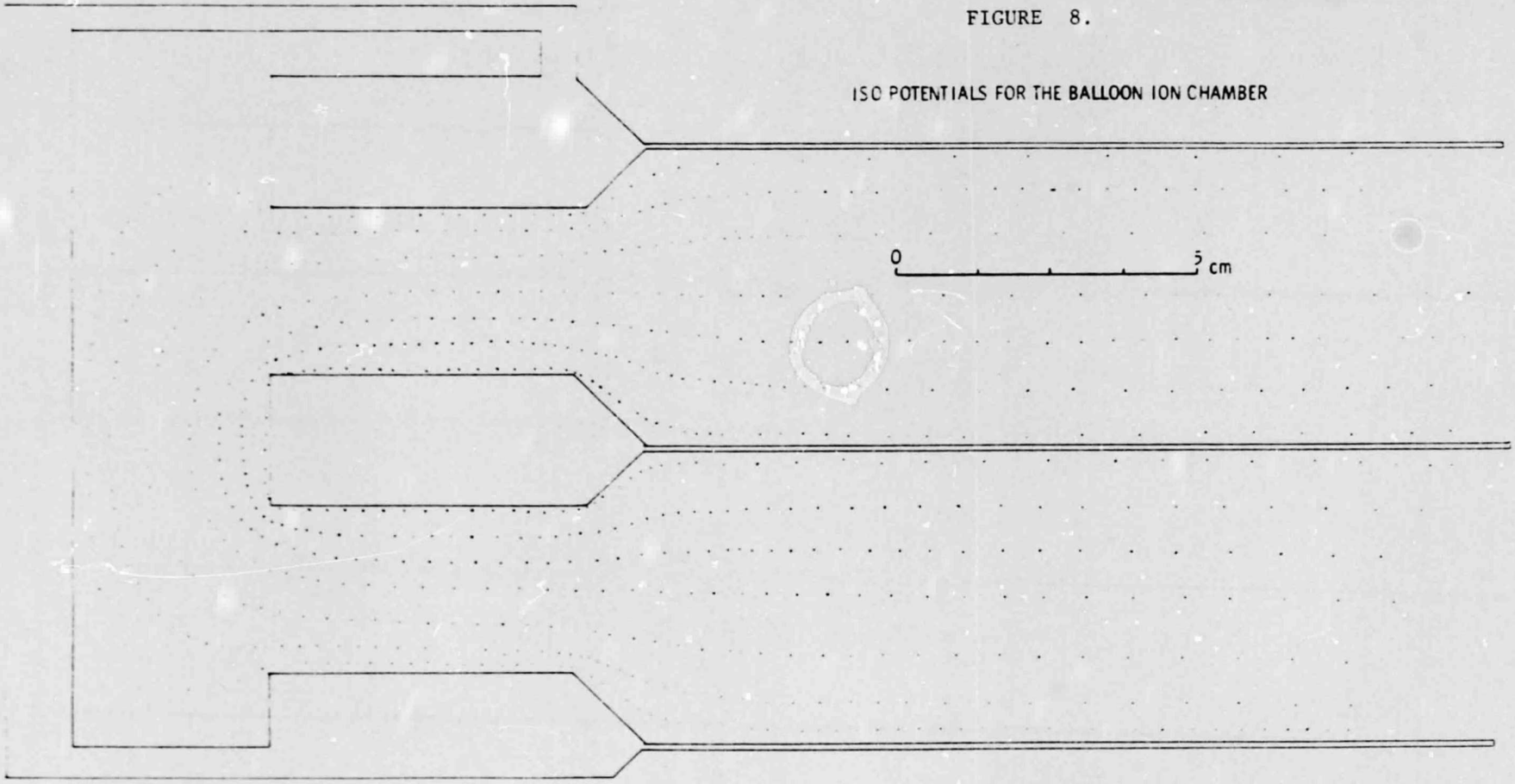

conducting paper as shown in Figure 8 and isopotential lines were constructed. It may be seen that at the edges of the active area the frames tend to pinch the isopotentials (increasing the field) in the middle of the gap and weaken the field in the corners. The two effects tend to cancel in their impact on charge collection efficiency. Estimated field purturbations are about ± 12% at 1 cm from the frame and ± 6% 2 cm from the frame. The accuracy of the plotting technique is not better than ± 2%. Possible reduction in charge pulse height for a particle track 2 cm from the edge of the active area is estimated to be no more than 0.25% and about twice this at 1 cm. from the edge.

Angular Uncertainty

The angle at which a particle passes through the stack of detectors is defined by the proportional counter hodoscopes. These are four x-y pairs in two sets of two pairs, the two sets being separated by 50 cm. Wire spacing between individual anodes is 0.5 cm. Angular resolution is ~ 1^{o} which produces negligible track length uncertainty in the ion chambers at angles close to the instrument axis (normal to the detector planes) but increasing to about 1% at maximum angle between track and axis.

Ion Chamber Gas Studies

Although there is a clear advantage in charge resolution of relativistic cosmic rays in using xenon as the chamber gas fill instead of argon, a series of tests were made with both these gases in various mixtures with such gases as CO_2 and CH_4 commonly used to moderate electron temperatures. The cylindrical test ion chamber used in these studies is shown in Figure 9. The chamber is constructed of stainless steel and has internal dimensions

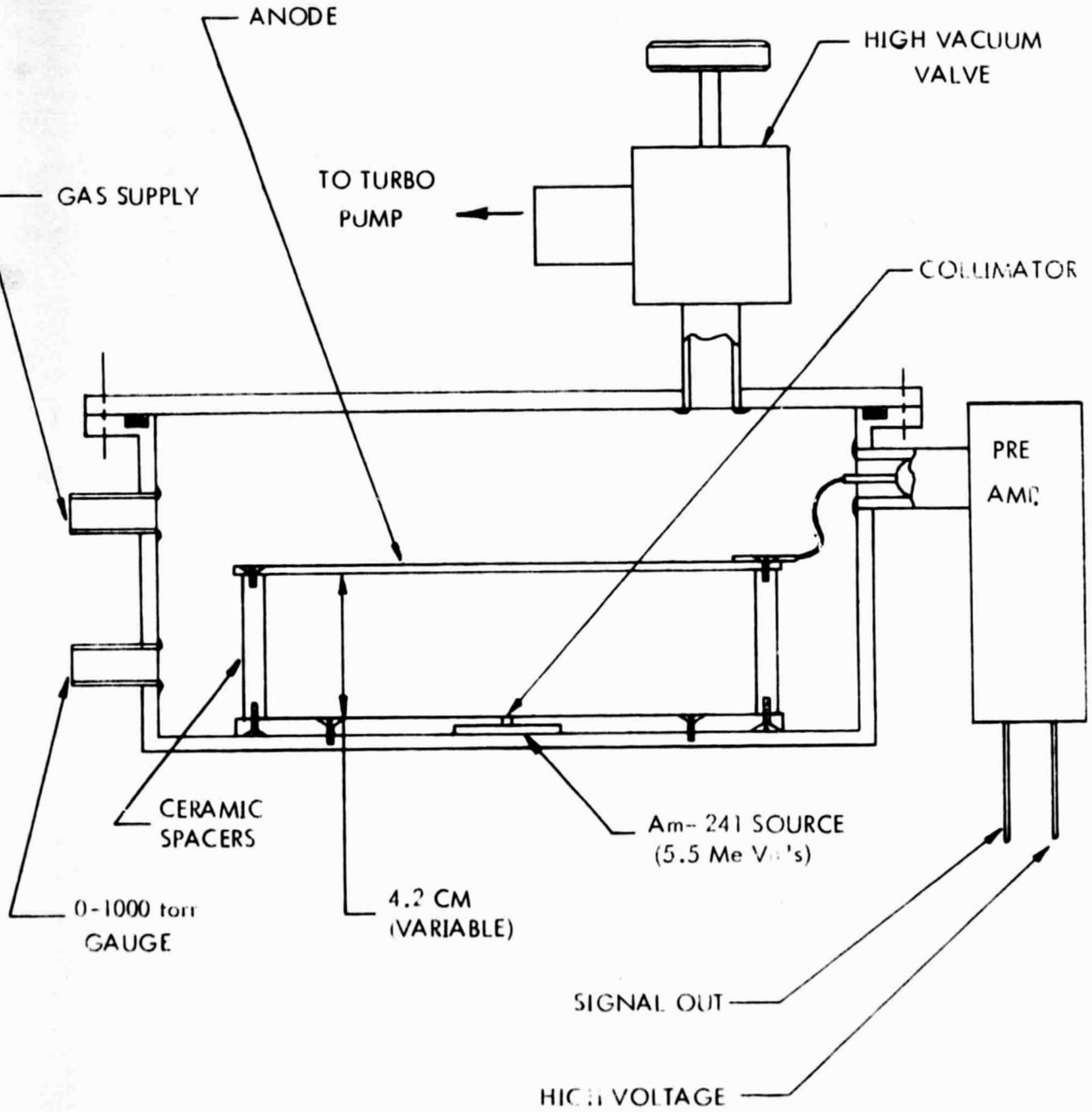

FIGURE 9

CYLINDRICAL TES[illegible] ION CHAMBER

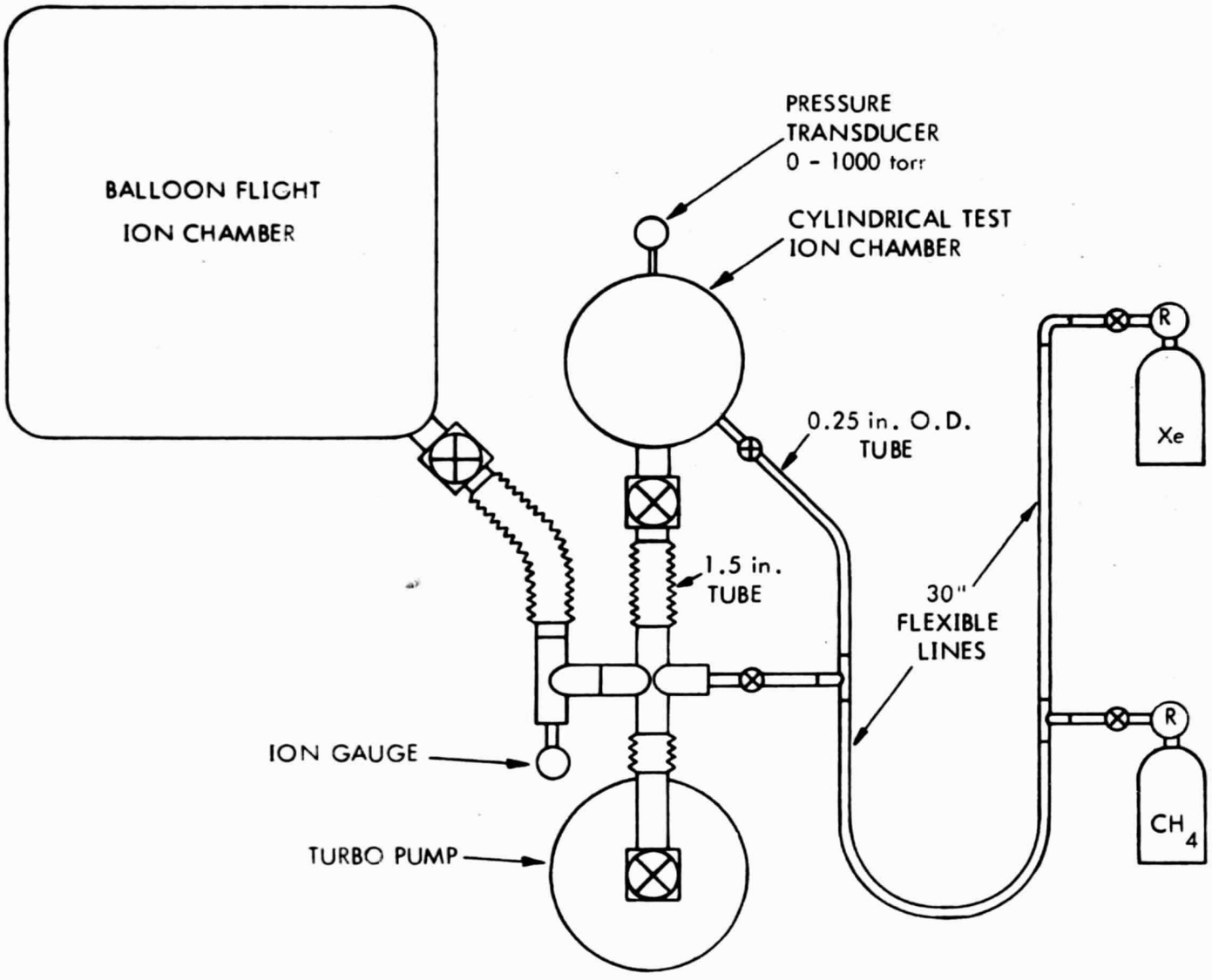

FIGURE 10. ION CHAMBER GAS-FILL SYSTEM

large proportion of the CO_2 remains in the tubing between the CO_2 regulator and the ion chamber, and erroneous readings will be obtained if one proceeds with the experiment. To prevent this problem from arising, the gas-fill line was made of 0.25 in diameter stainless steel tubing to minimise its volume, and the pressure in the ion chamber was lowered about 10% before admitting CO_2. After adjusting the partial pressure of CO_2 in the ion chamber to the new value, the total pressure in the chamber was returned to 760 torr with xenon. This had the effect of sweeping any CO_2 in the inlet manifold into the chamber ensuring that the chamber contained the calculated proportions of the two gases.

The distribution of pulse heights for 5.5 MeV α's in the gas mixture was then obtained at anode voltages from 0-1200V. The channel number of the center of the peak of these distributions was plotted against applied voltage. These plots, together with pulse risetime as a function of anode voltage are shown for mixtures of $Ar-CO_2$, $Xe-CO_2$, and $Xe-CH_4$ between 1 and 10% of the quench gas; (see Figures 11-21). The data for the argon mixtures is shown for various values of amplifier shaping time, and pulse height clipping is evident where the shaping time is too short.

Gas Contamination Effects on Charge Collection Efficiency

Ion chambers are normally operated in the plateau region, which name refers to the plot of collected charge versus voltage applied. In this region of several hundred volts, essentially all the electronic charge is collected within several microseconds. The height, slope and onset voltage of this plateau are effected by gas contaminants, and the effects appear more pronounced with Xe then with Ar since the electronic drift velocity is lower in Xe. Charge losses may be either by columnar recombination, or by

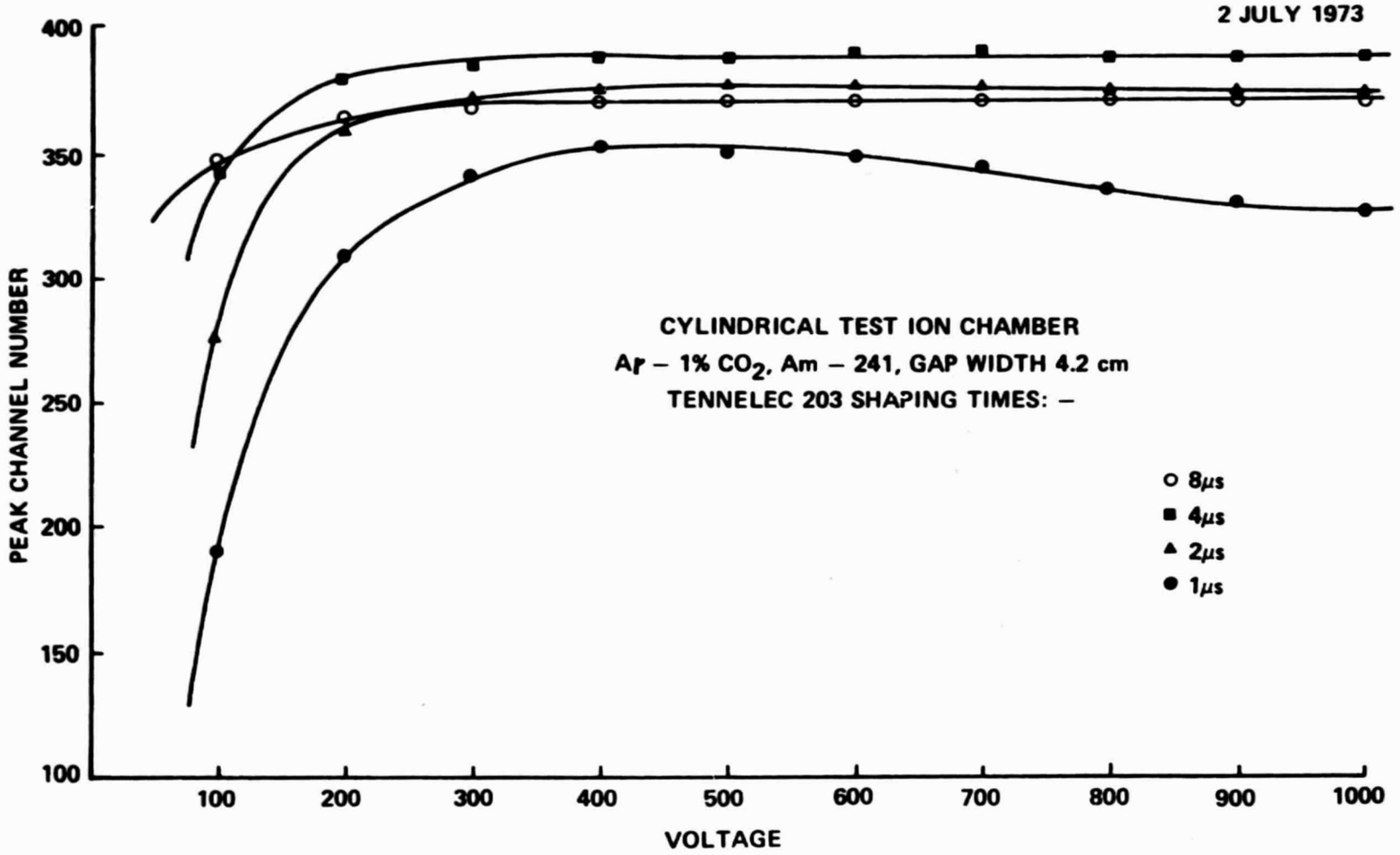
2 JULY 1973
CYLINDRICAL TEST ION CHAMBER
Ar – 1% CO_2, Am – 241, GAP WIDTH 4.2 cm
TENNELEC 203 SHAPING TIMES: –
8μs
4μs
2μs
1μs
PEAK CHANNEL NUMBER
VOLTAGE
400
350
300
250
200
150
100
100
200
300
400
500
600
700
800
900
1000

FIGURE 11.

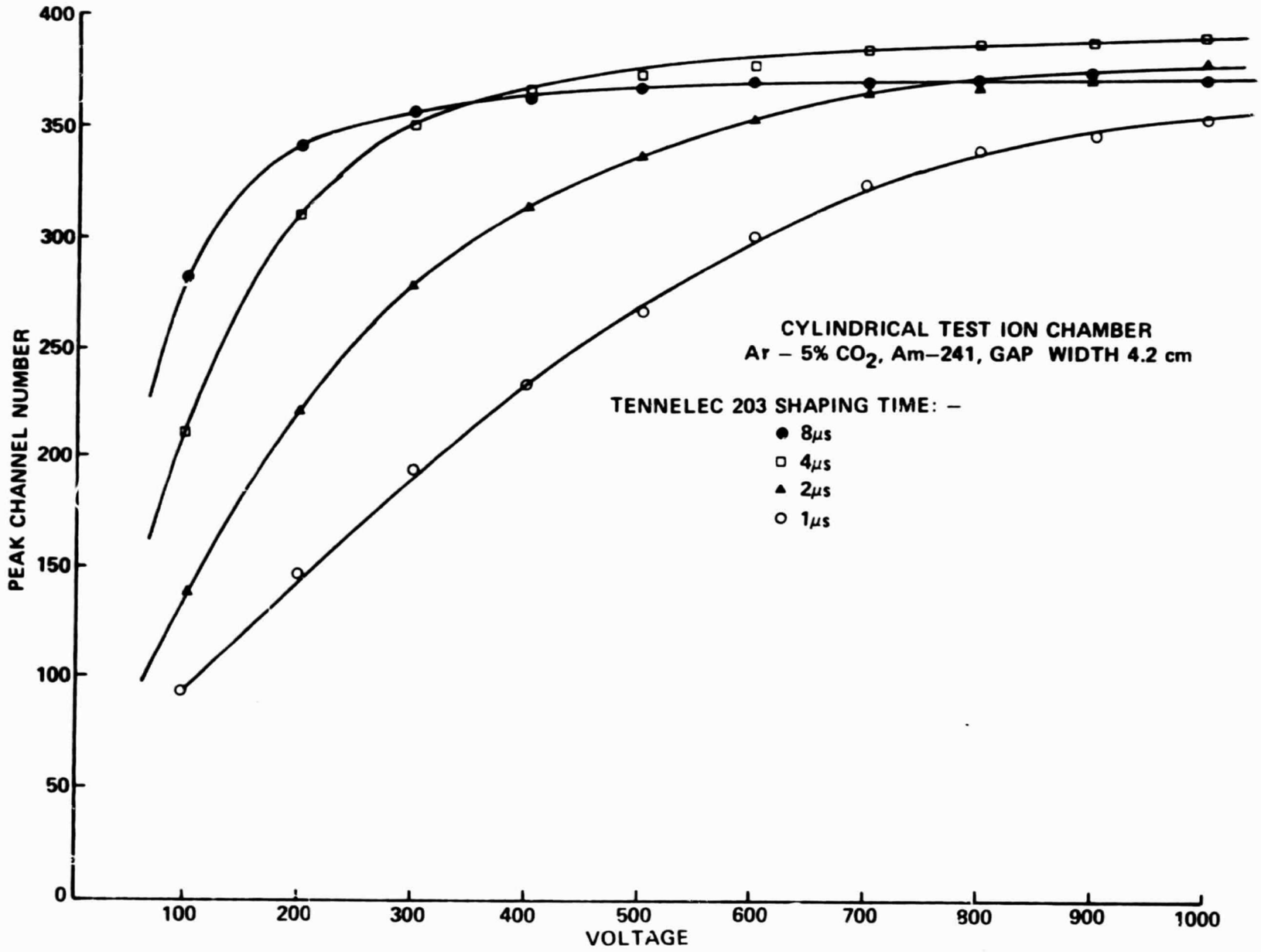
CYLINDRICAL TEST ION CHAMBER
Ar – 5% CO_2, Am–241, GAP WIDTH 4.2 cm
TENNELEC 203 SHAPING TIME: –
● 8μs
□ 4μs
▲ 2μs
○ 1μs
PEAK CHANNEL NUMBER
VOLTAGE
0
50
100
150
200
250
300
350
400
100
200
300
400
500
600
700
800
900
1000

FIGURE 12.

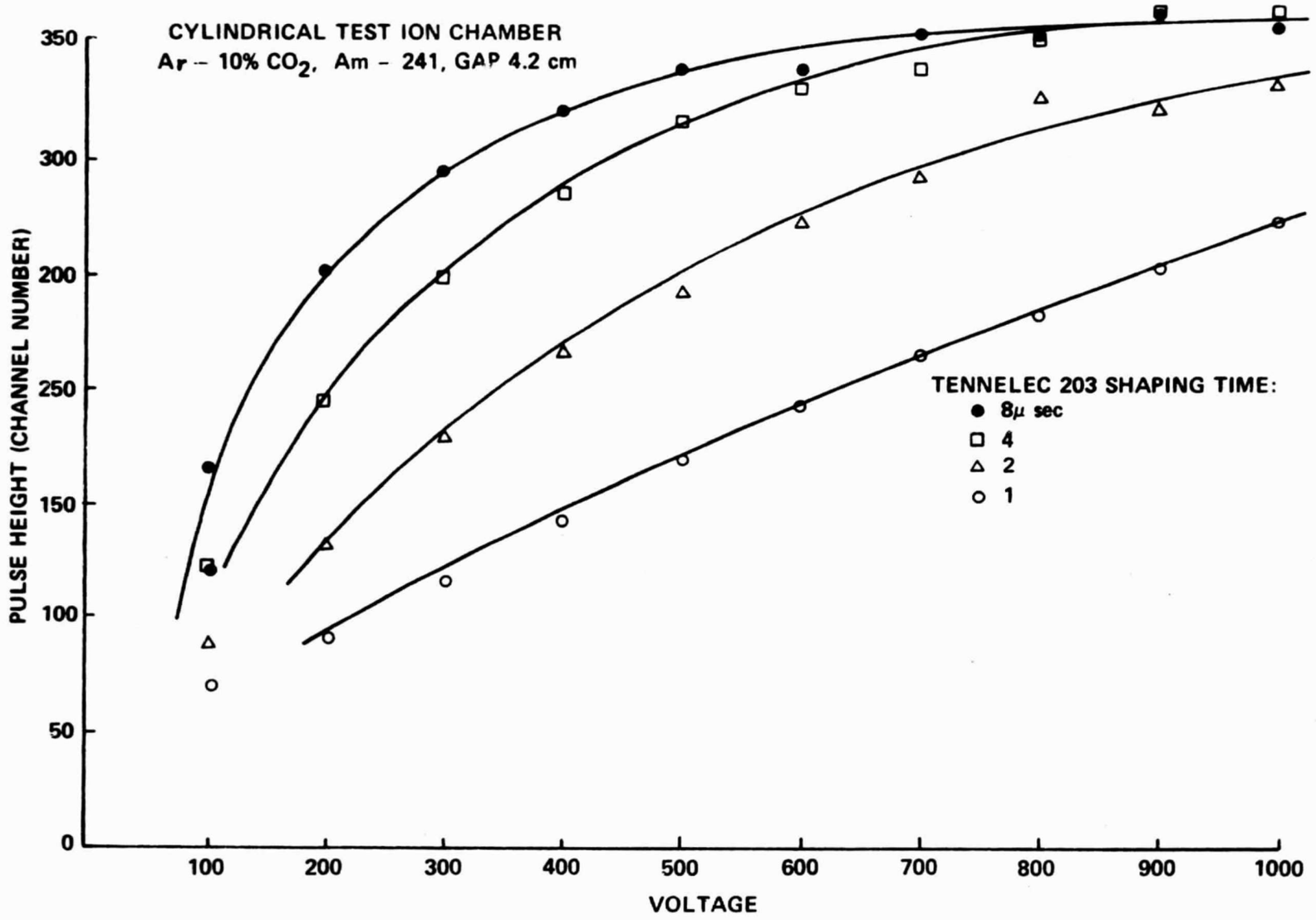
CYLINDRICAL TEST ION CHAMBER
Ar – 10% CO_2, Am – 241, GAP 4.2 cm
PULSE HEIGHT (CHANNEL NUMBER)
VOLTAGE
TENNELEC 203 SHAPING TIME:
8μ sec
4
2
1
0
50
100
150
200
250
300
350
100
200
300
400
500
600
700
800
900
1000

FIGURE 13.

FIGURE 14.

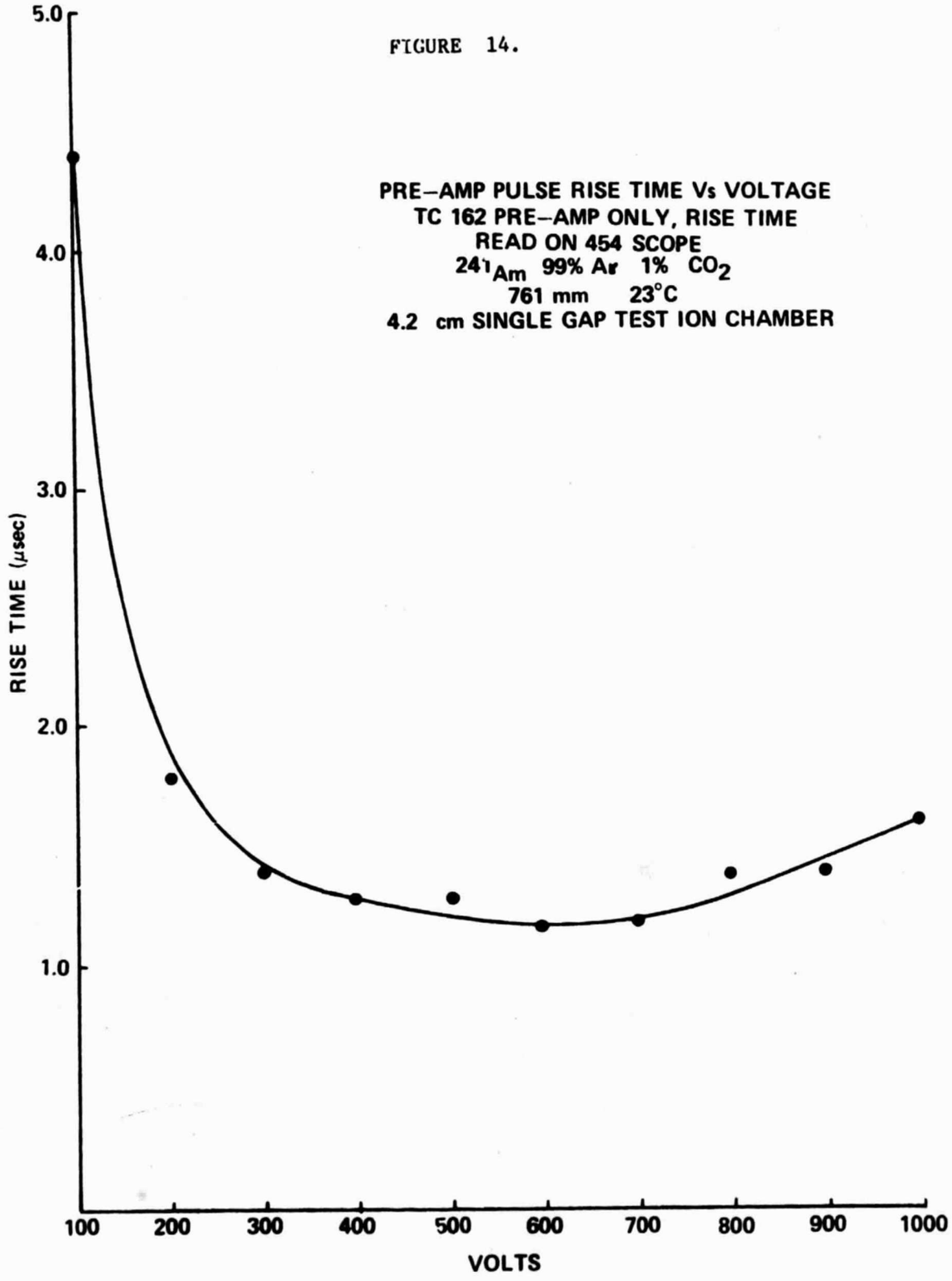
PRE–AMP PULSE RISE TIME Vs VOLTAGE
TC 162 PRE–AMP ONLY, RISE TIME
READ ON 454 SCOPE
^{241}Am 99% Ar 1% CO_2
761 mm 23°C
4.2 cm SINGLE GAP TEST ION CHAMBER
RISE TIME (μsec)
5.0
4.0
3.0
2.0
1.0
100
200
300
400
500
600
700
800
900
1000
VOLTS

FIGURE 15.

RISE TIME OF PRE–AMP PULSE VS H.V.
TC 162 PRE–AMP ONLY, RISE TIME
READ ON 454 SCOPE
^{241}Am 95% Ar 5% CO_2
756 mm 22°C
4.2 cm SINGLE GAP TEST ION CHAMBER

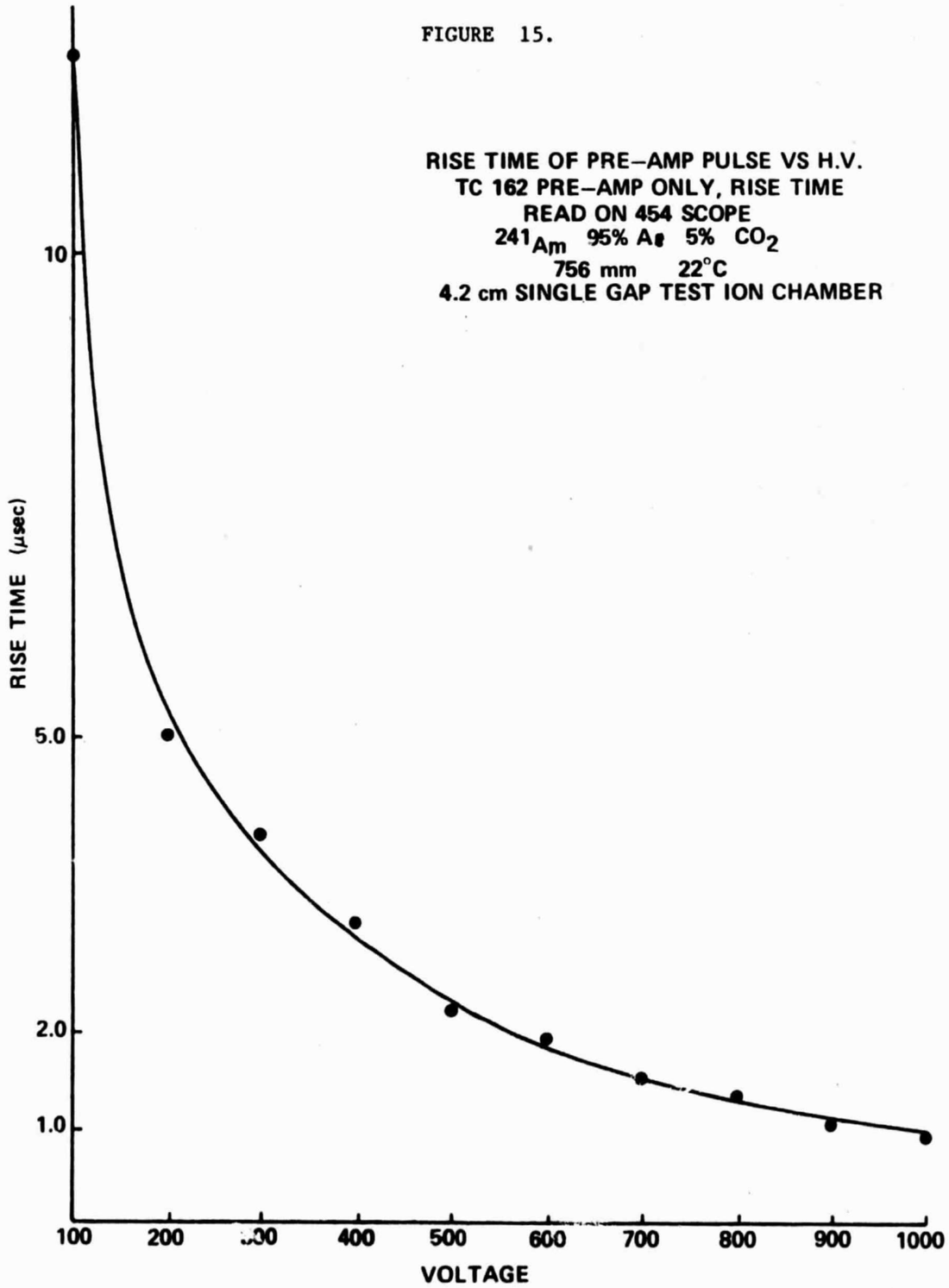

FIGURE 16.

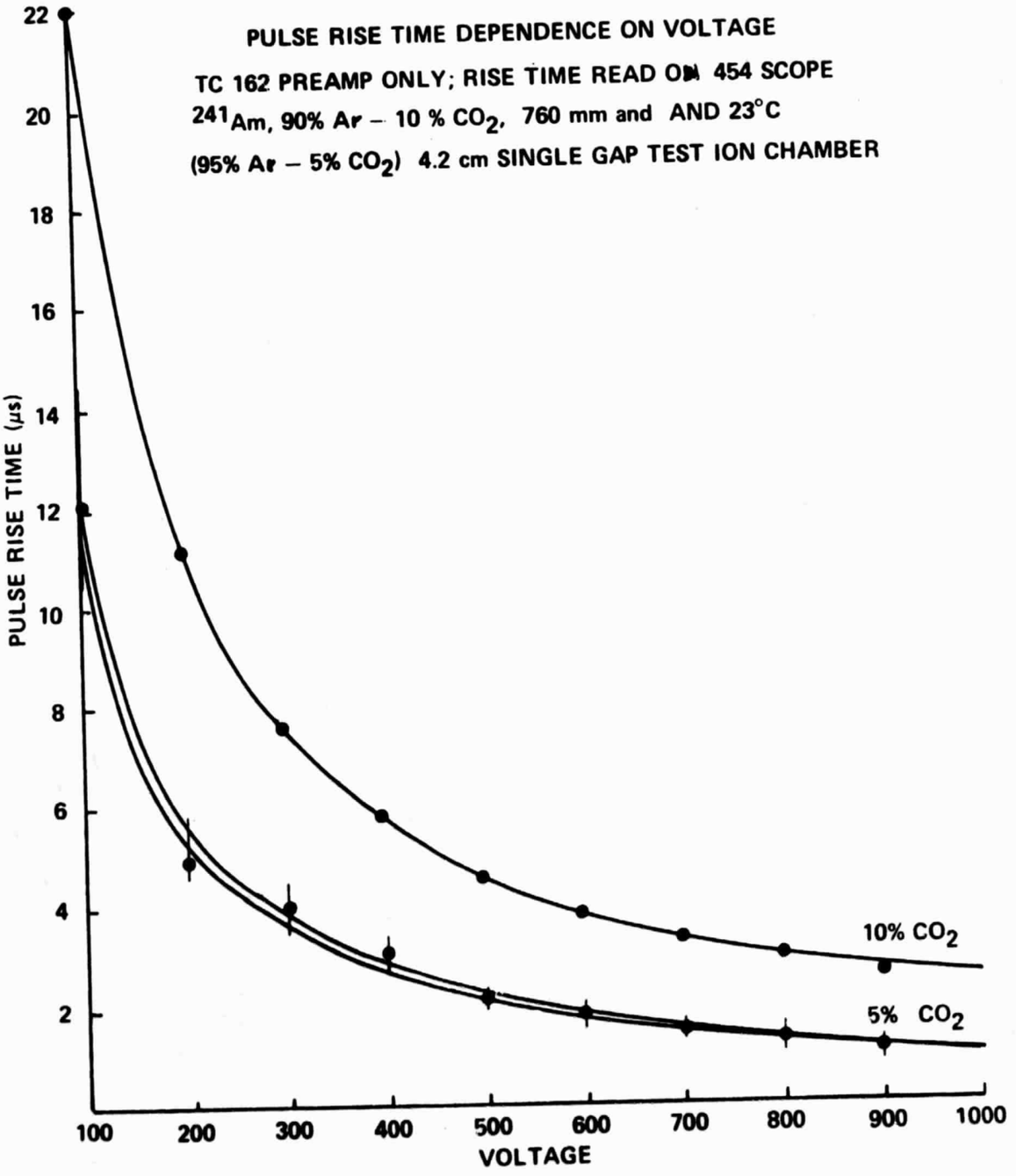
PULSE RISE TIME DEPENDENCE ON VOLTAGE
TC 162 PREAMP ONLY; RISE TIME READ ON 454 SCOPE
241Am, 90% Ar – 10 % CO2, 760 mm and AND 23°C
(95% Ar – 5% CO2) 4.2 cm SINGLE GAP TEST ION CHAMBER
PULSE RISE TIME (μs)
22
20
18
16
14
12
10
8
6
4
2
100
200
300
400
500
600
700
800
900
1000
VOLTAGE
10% CO2
5% CO2

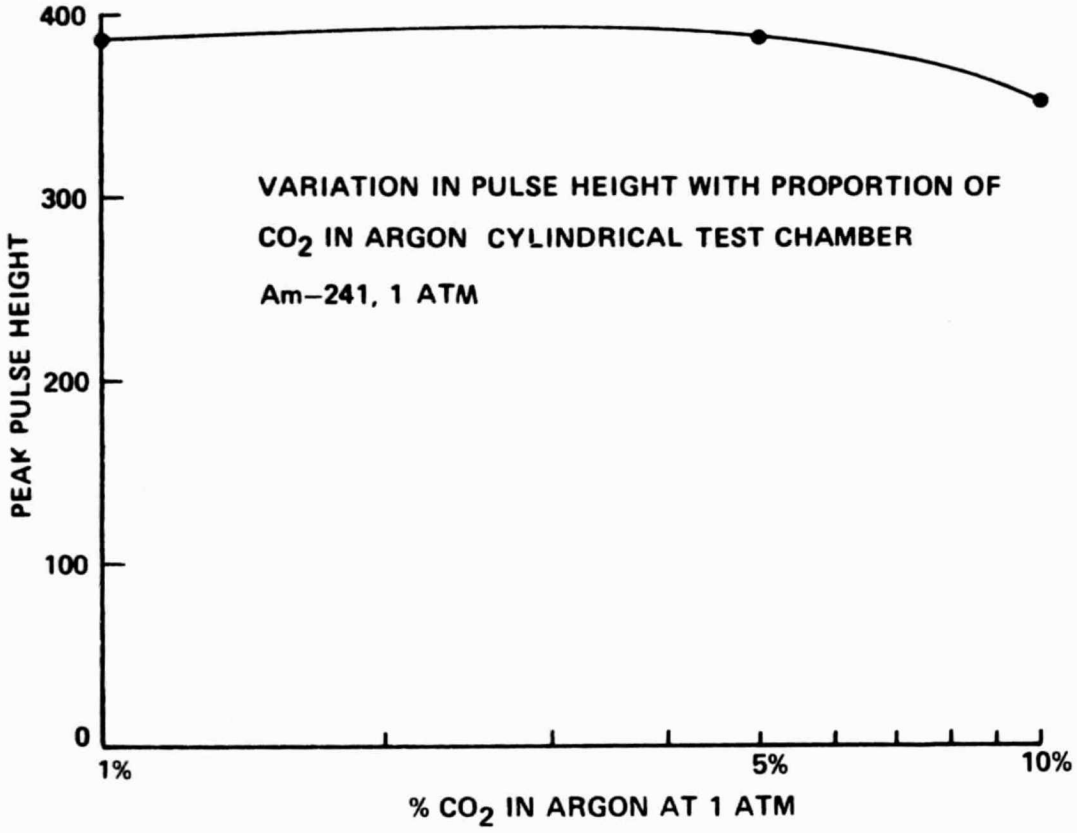
400
300
200
100
0
PEAK PULSE HEIGHT
VARIATION IN PULSE HEIGHT WITH PROPORTION OF
CO_2 IN ARGON CYLINDRICAL TEST CHAMBER
Am–241, 1 ATM
1%
5%
10%
% CO_2 IN ARGON AT 1 ATM

FIGURE 17.

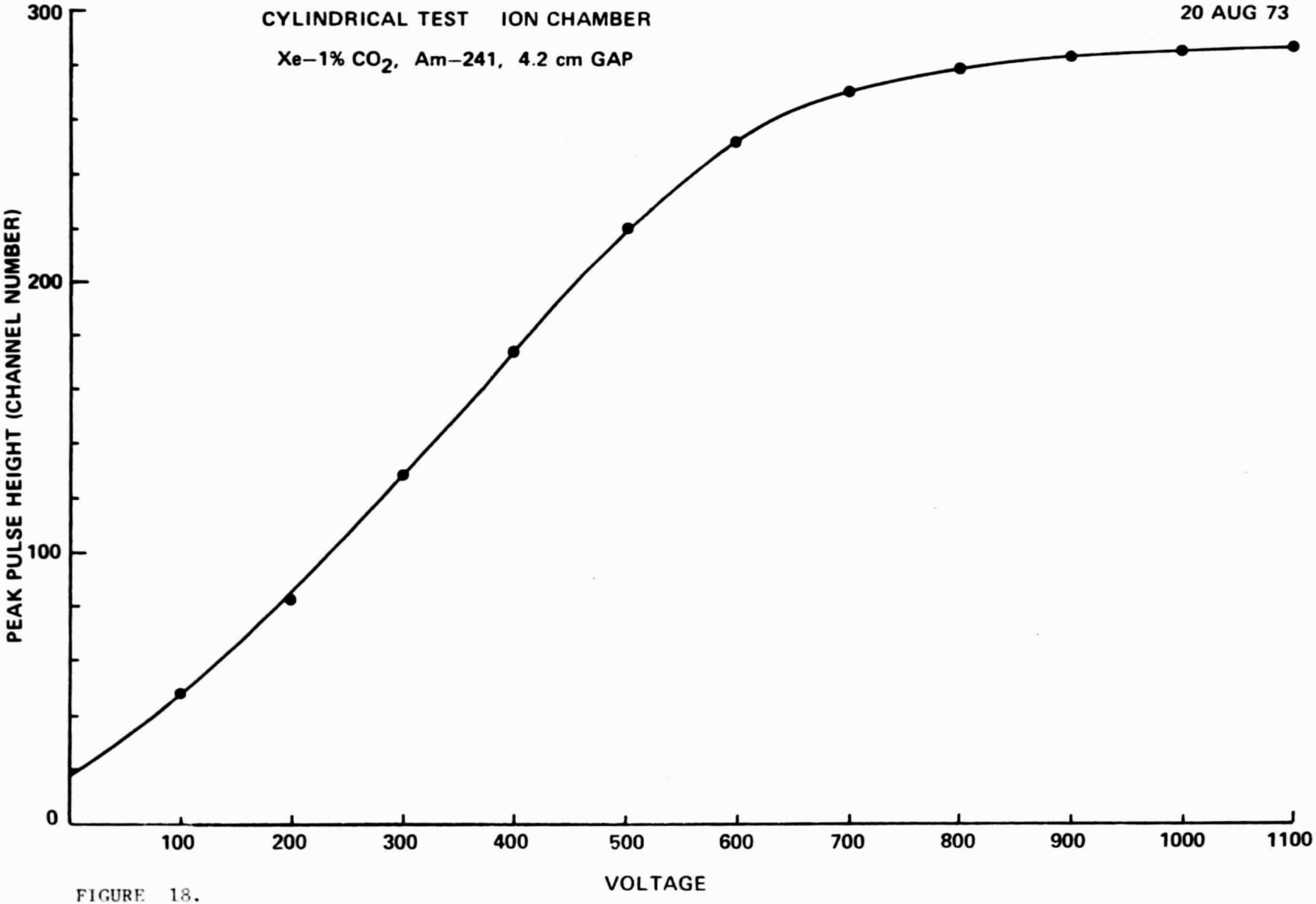
CYLINDRICAL TEST ION CHAMBER
Xe–1% CO_2, Am–241, 4.2 cm GAP
20 AUG 73
PEAK PULSE HEIGHT (CHANNEL NUMBER)
300
200
100
0
100
200
300
400
500
600
700
800
900
1000
1100
VOLTAGE

FIGURE 18.

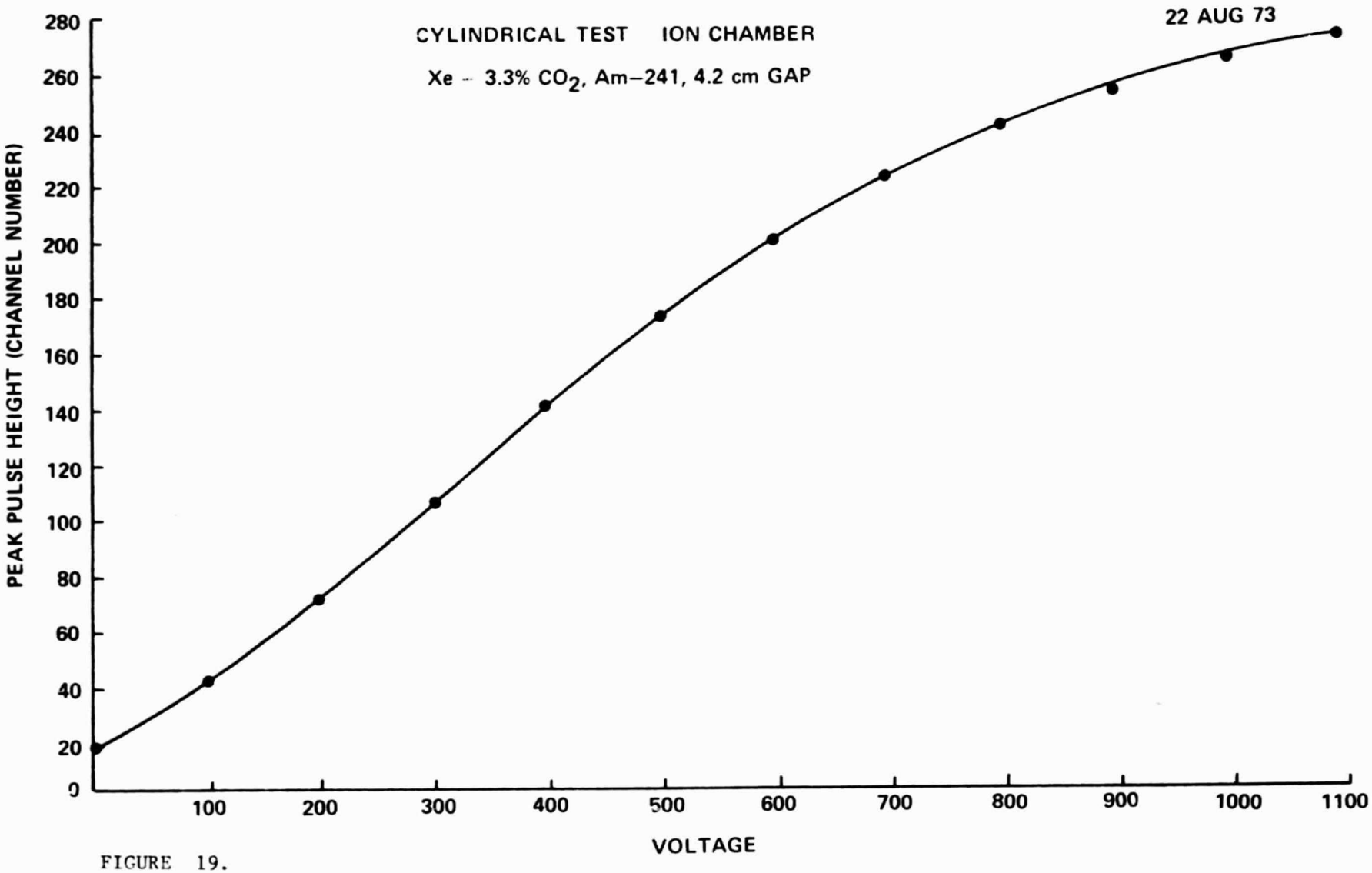
CYLINDRICAL TEST ION CHAMBER
Xe – 3.3% CO_2, Am–241, 4.2 cm GAP
22 AUG 73
PEAK PULSE HEIGHT (CHANNEL NUMBER)
280
260
240
220
200
180
160
140
120
100
80
60
40
20
0
100
200
300
400
500
600
700
800
900
1000
1100
VOLTAGE

FIGURE 19.

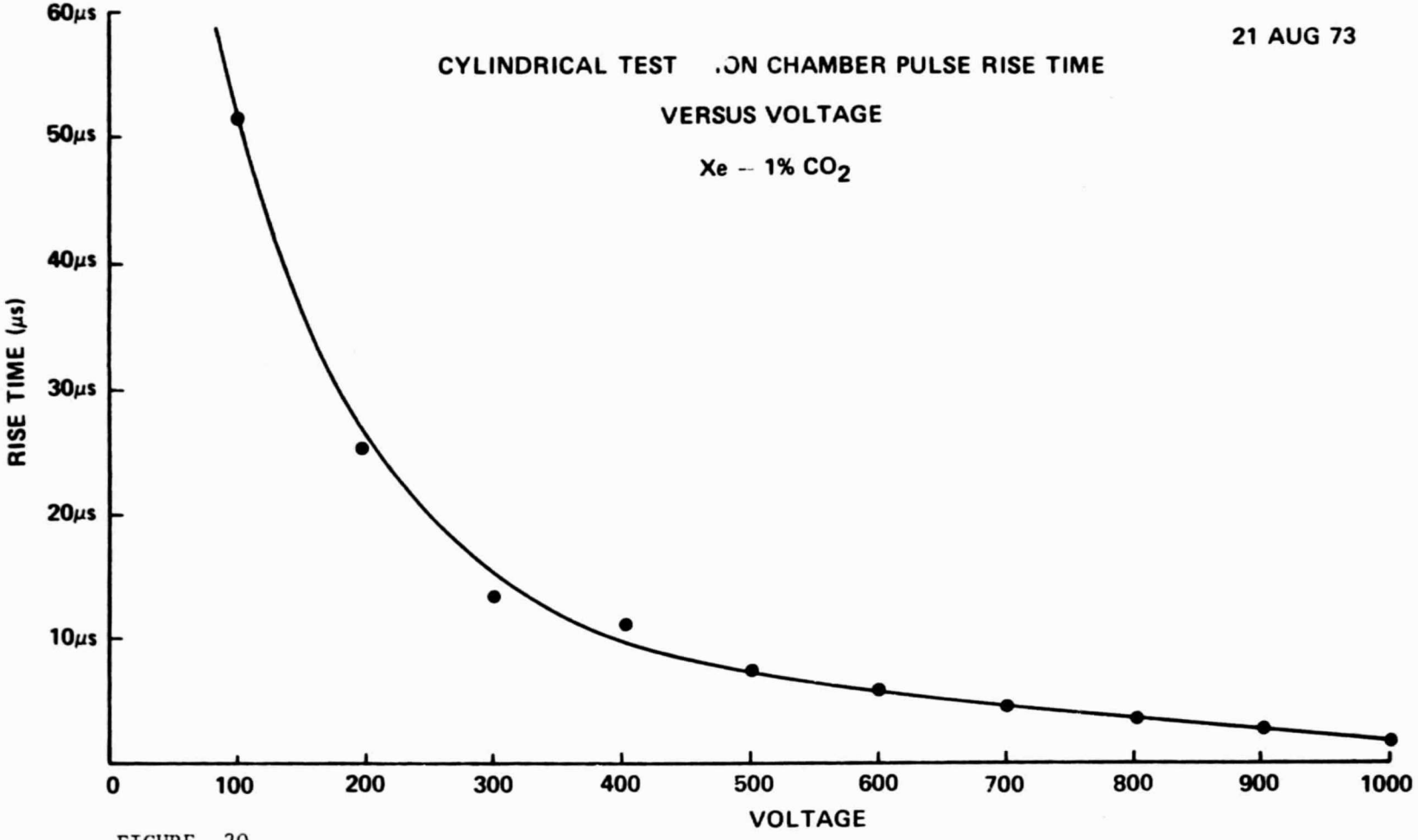
21 AUG 73
CYLINDRICAL TEST .ON CHAMBER PULSE RISE TIME
VERSUS VOLTAGE
Xe -- 1% CO_2
RISE TIME (μs)
60μs
50μs
40μs
30μs
20μs
10μs
0
100
200
300
400
500
600
700
800
900
1000
VOLTAGE

FIGURE 20.

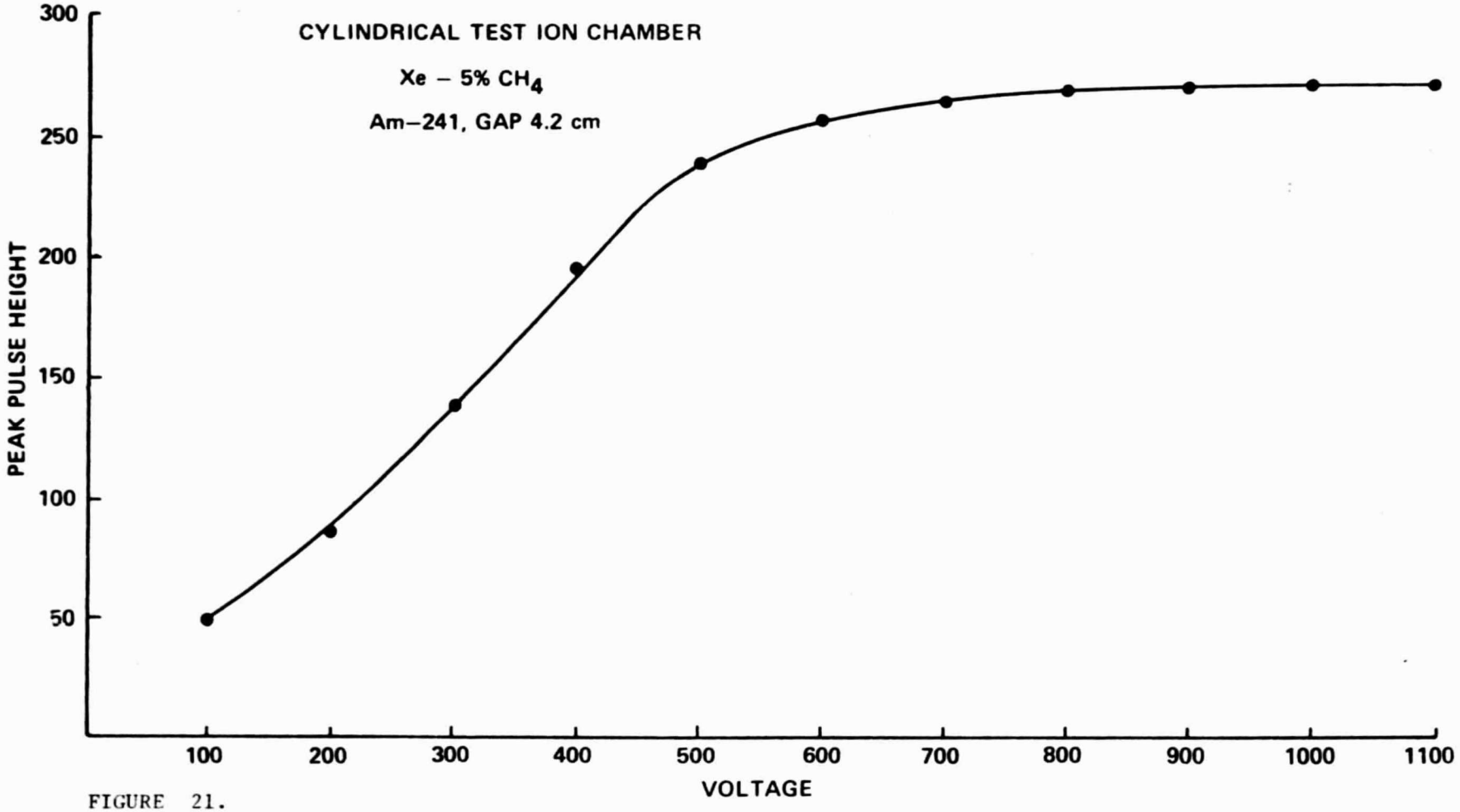
CYLINDRICAL TEST ION CHAMBER
Xe – 5% CH_4
Am–241, GAP 4.2 cm
PEAK PULSE HEIGHT
300
250
200
150
100
50
100
200
300
400
500
600
700
800
900
1000
1100
VOLTAGE

FIGURE 21.

electron capture: the latter reducing the drift velocity of the charge to the anode so that the fast electronics rejects it. Columnar recombination between electrons and positive ions has not been adequately treated. Jaffe's treatment is of recombination between negative and positive ions and requires that electrons be rapidly captured before they leave the track core. Electron capture and columnar recombination may be differentiated by careful experimentation.

The migration of electrons in pulse ion chambers is strongly dependent on the composition of the gas. Not only does the drift velocity or collection time vary with the inert gas used but it is critically affected by small concentrations of electronegative gases. The importance of quantifying and then controlling or predicting these effects is of great importance for gas filled detectors designed for long space flight, such as those which form part of some HEAO experiments. An example of the effects of contamination on the performance of the cylindrical test ion chamber over an extended period is shown in Figure 22. This behavior is worse than we have obtained with the large area balloon chambers. Limited data for these is shown in Figure 23. In this case a peak pulse height versus voltage curve was not obtained, merely the peak pulse height at 1000V. Complete voltage characteristics are given for two dates 6 months apart in Figure 24 and 25 for the same xenon-methane gas fill. The same plot is shown for a new gas fill into the same ion chambers in Figures 26 and 27. The chambers were pumped out and leak checked between fills without exposing the interior surfaces to the atmosphere at any time. Subsequent data after April 1974 show a slower deterioration than for the September 1973 gas fill. Two effects are noticeable. Firstly, the level of the plateau falls with the charge collection efficiency. This is not a serious problem except at low

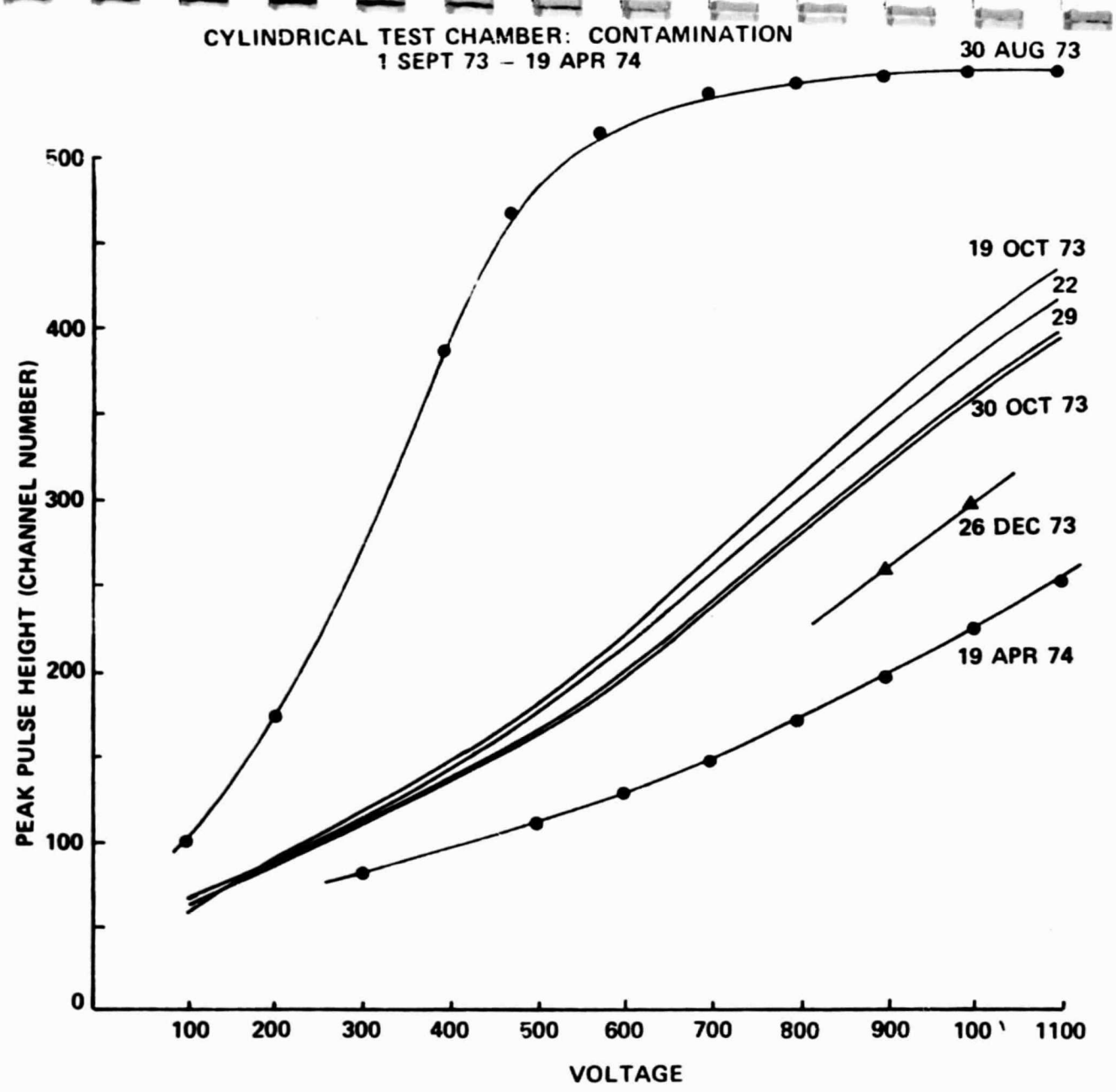
CYLINDRICAL TEST CHAMBER: CONTAMINATION
1 SEPT 73 – 19 APR 74
30 AUG 73
19 OCT 73
22
29
30 OCT 73
26 DEC 73
19 APR 74
PEAK PULSE HEIGHT (CHANNEL NUMBER)
0
100
200
300
400
500
100
200
300
400
500
600
700
800
900
1100
VOLTAGE

FIGURE 22.

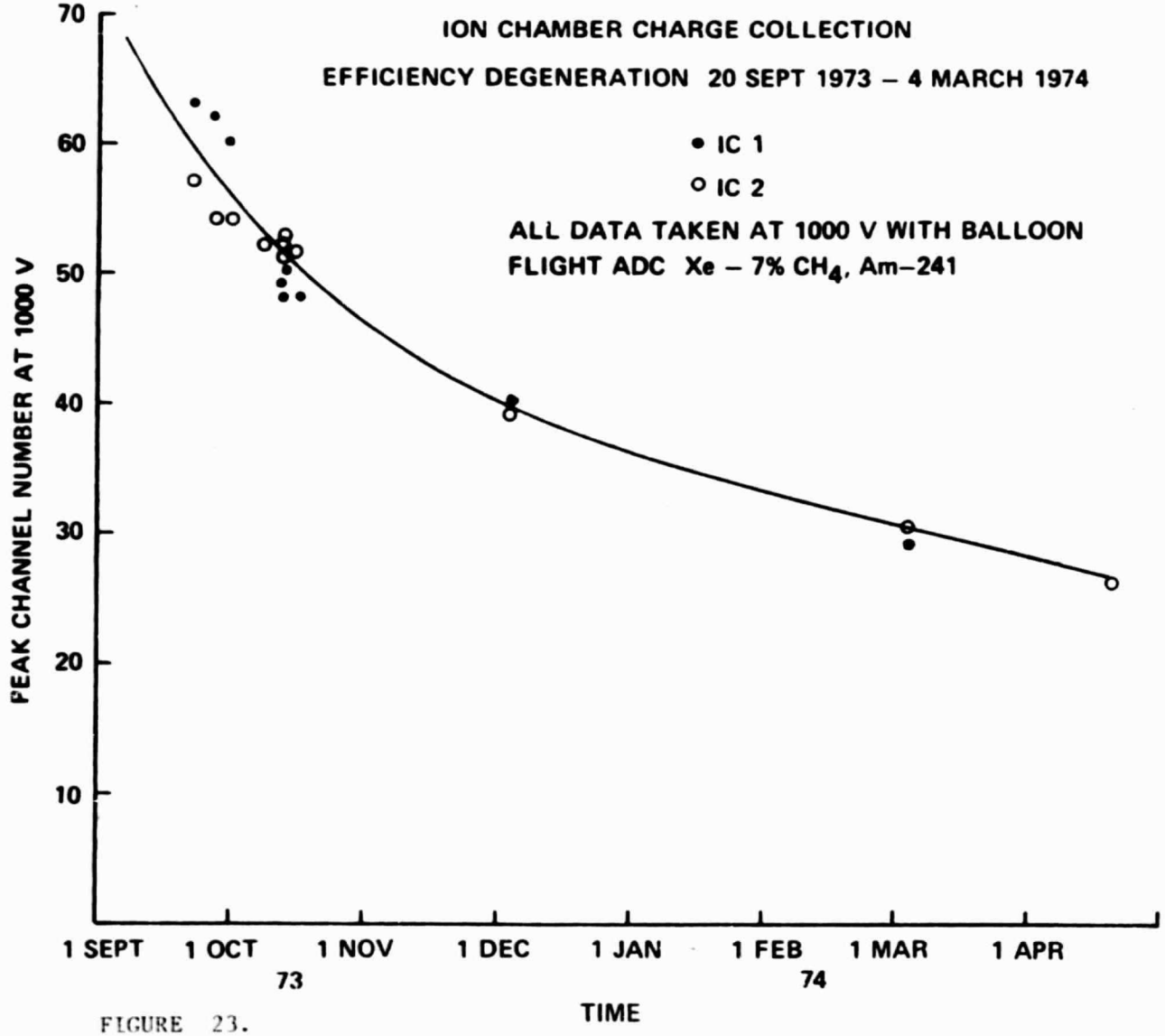
ION CHAMBER CHARGE COLLECTION
EFFICIENCY DEGENERATION 20 SEPT 1973 – 4 MARCH 1974
• IC 1
○ IC 2
ALL DATA TAKEN AT 1000 V WITH BALLOON
FLIGHT ADC Xe – 7% CH_4, Am–241
PEAK CHANNEL NUMBER AT 1000 V
70
60
50
40
30
20
10
1 SEPT
1 OCT
1 NOV
1 DEC
1 JAN
1 FEB
1 MAR
1 APR
73
74
TIME

FIGURE 23.

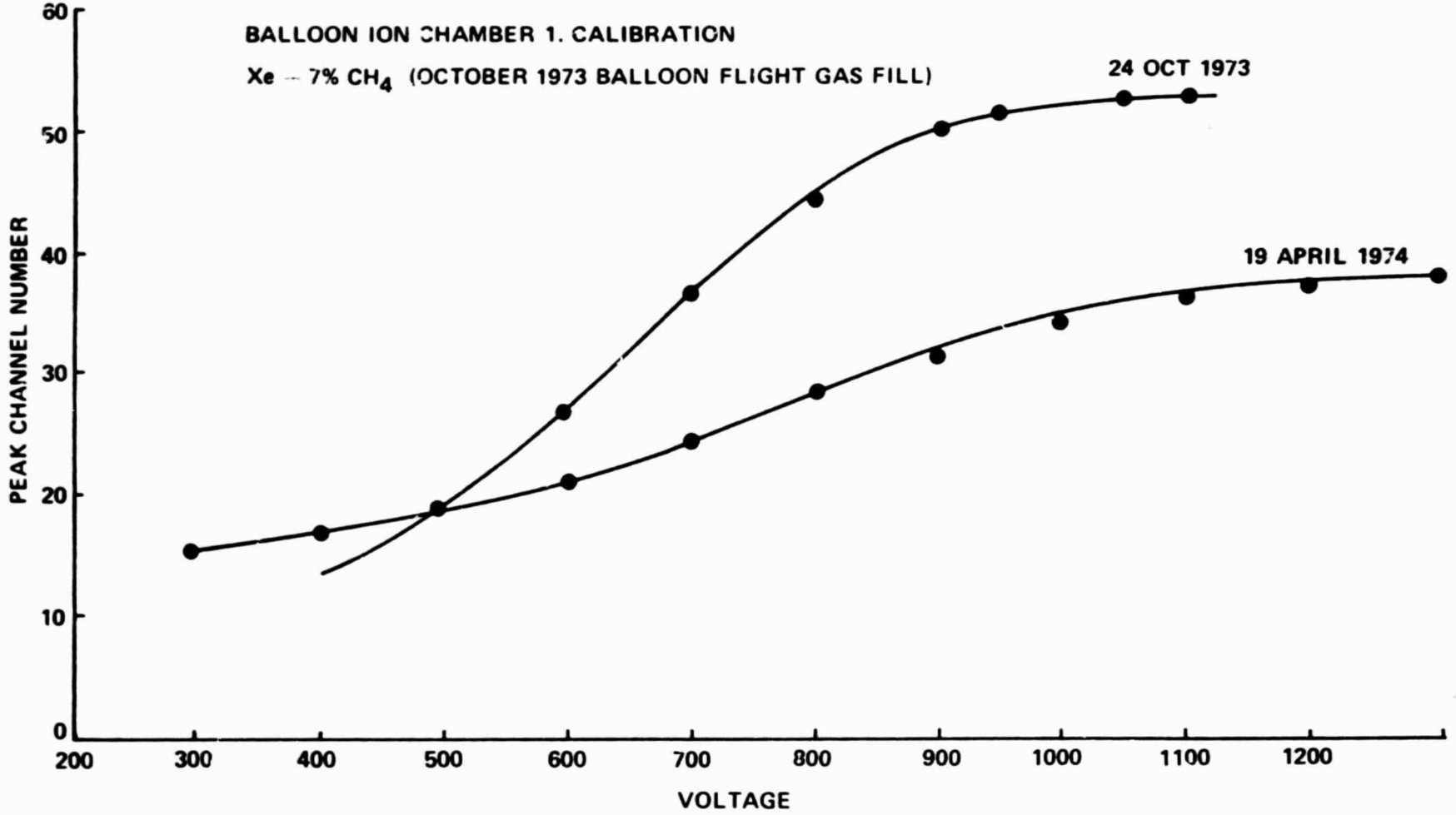
BALLOON ION CHAMBER 1. CALIBRATION
Xe – 7% CH_4 (OCTOBER 1973 BALLOON FLIGHT GAS FILL)
24 OCT 1973
19 APRIL 1974
PEAK CHANNEL NUMBER
VOLTAGE
0
10
20
30
40
50
60
200
300
400
500
600
700
800
900
1000
1100
1200

FIGURE 24.

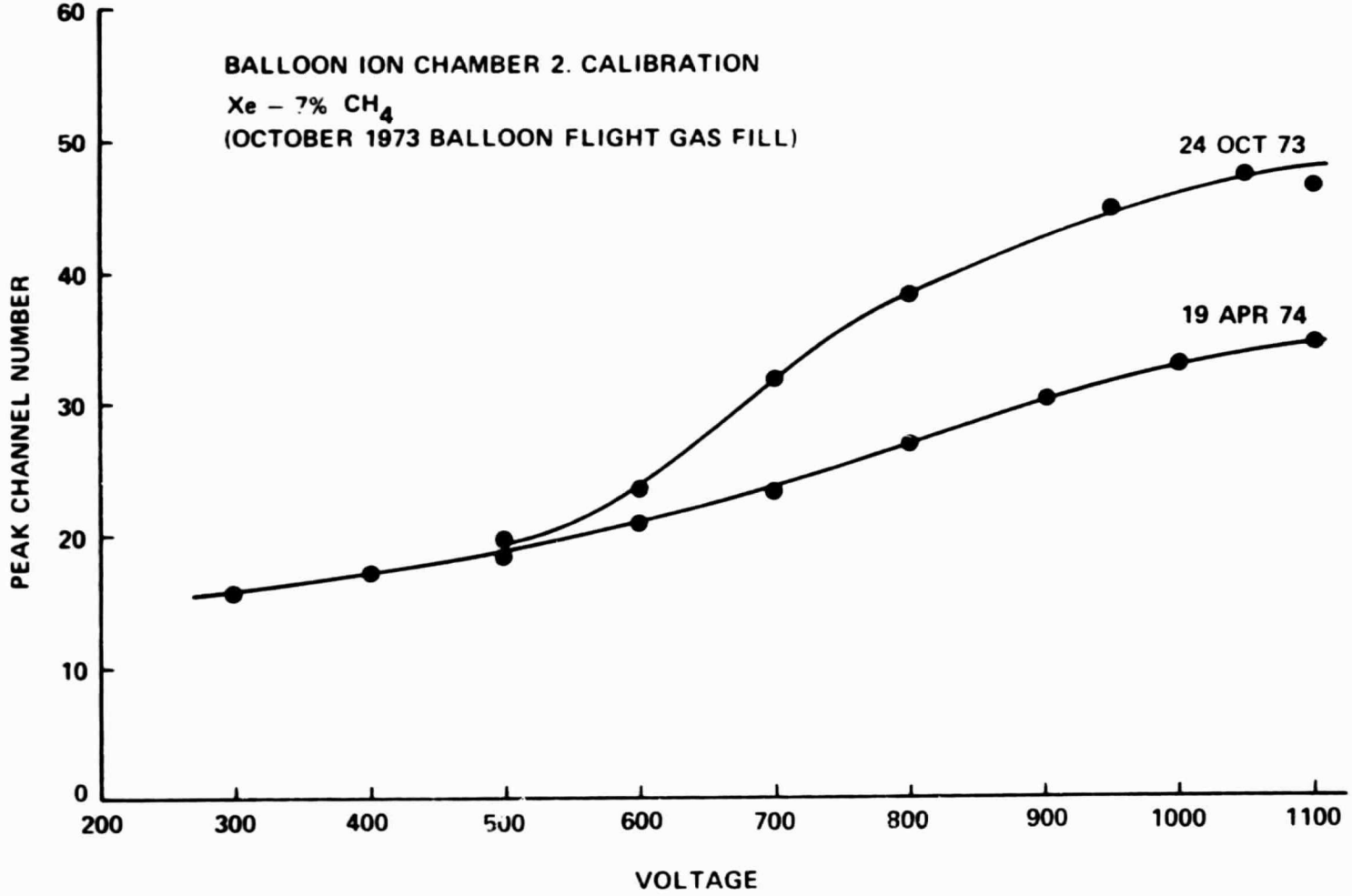
BALLOON ION CHAMBER 2. CALIBRATION
Xe – 7% CH_4
(OCTOBER 1973 BALLOON FLIGHT GAS FILL)
24 OCT 73
19 APR 74
PEAK CHANNEL NUMBER
VOLTAGE
0
10
20
30
40
50
60
200
300
400
500
600
700
800
900
1000
1100

FIGURE 25

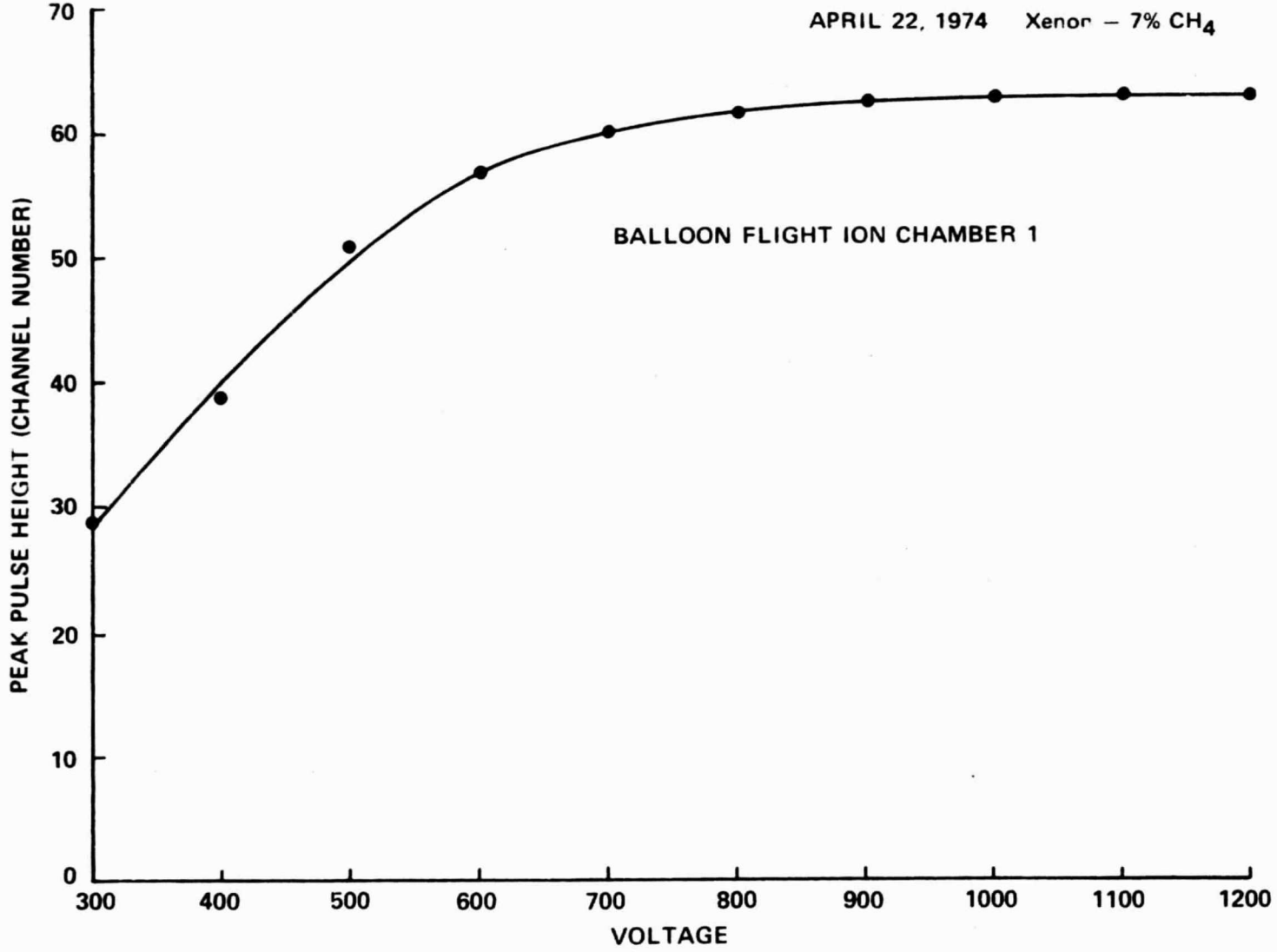
APRIL 22, 1974 Xenor – 7% CH_4
BALLOON FLIGHT ION CHAMBER 1
PEAK PULSE HEIGHT (CHANNEL NUMBER)
VOLTAGE
0
10
20
30
40
50
60
70
300
400
500
600
700
800
900
1000
1100
1200

FIGURE 26.

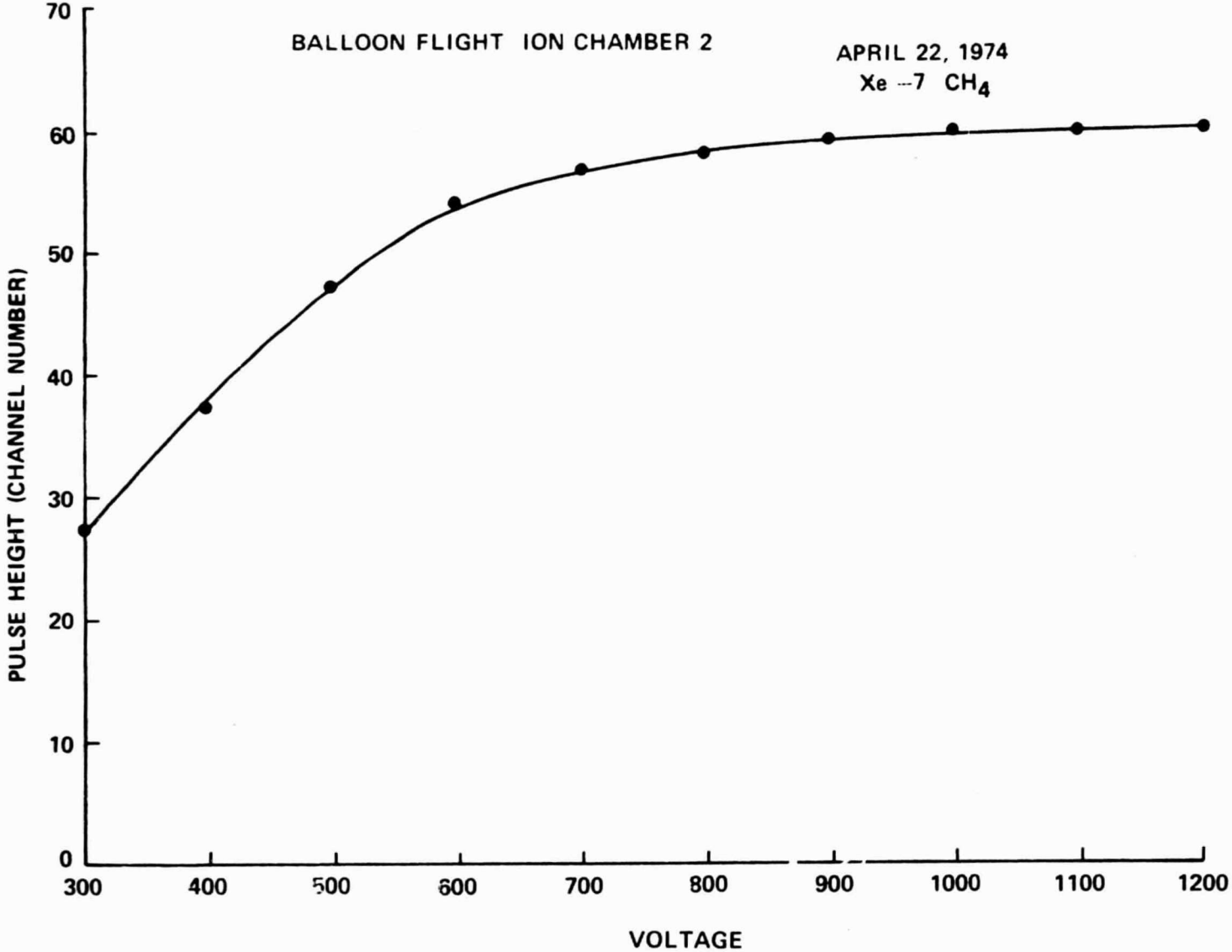
BALLOON FLIGHT ION CHAMBER 2
APRIL 22, 1974
Xe --7 CH_4
PULSE HEIGHT (CHANNEL NUMBER)
70
60
50
40
30
20
10
0
300
400
500
600
700
800
900
1000
1100
1200
VOLTAGE

FIGURE 27.

z since intermittent calibrations should always be performed. Broadening of the distribution must occur, however, due to poorer statistics. Secondly, the plateau threshold moves to the right so that the operating voltage is no longer on it. In this case field variations within the active volume will also cause charge resolution degradation.

Pulse Risetimes

Risetimes were measured at the Tennelec preamplfier output and constitute the time taken for the pulse to rise between 10% and 90% of its full value. The measurements were made from photographs of the oscilloscope screen and in some cases, as noted on the figures, by direct inspection of the screen. There is excellent quantitative agreement between measured risetimes in all three argon-CO_2 mixtures and those calculated from the drift velocities given by English and Hanna (1953). Agreement between the two data sets for xenon-CO_2 mixtures is only qualitative, which is probably due to the short α-track length in xenon.

Pressure Dependence of Pulse Height

An experiment was conducted with the cylindrical test ion chamber to measure the gas pressure dependence of charge collection efficiency. The gas used was Ar-10% CO_2 with gap width of 4.2 cm and a collimated Am-241 source. Other operating conditions and the results are shown in Figure 28. It may be seen that the charge pulse corresponding to an americium α-particle is fairly constant around and above 1 standard atmosphere. The pulse height varies ± 1% with a variation in pressure of ± 4% (or ± 30 torr). Since the pressure in the ion chambers is normally adjusted to within 1 torr, pressure variation is not considered a problem for a charge collection. It

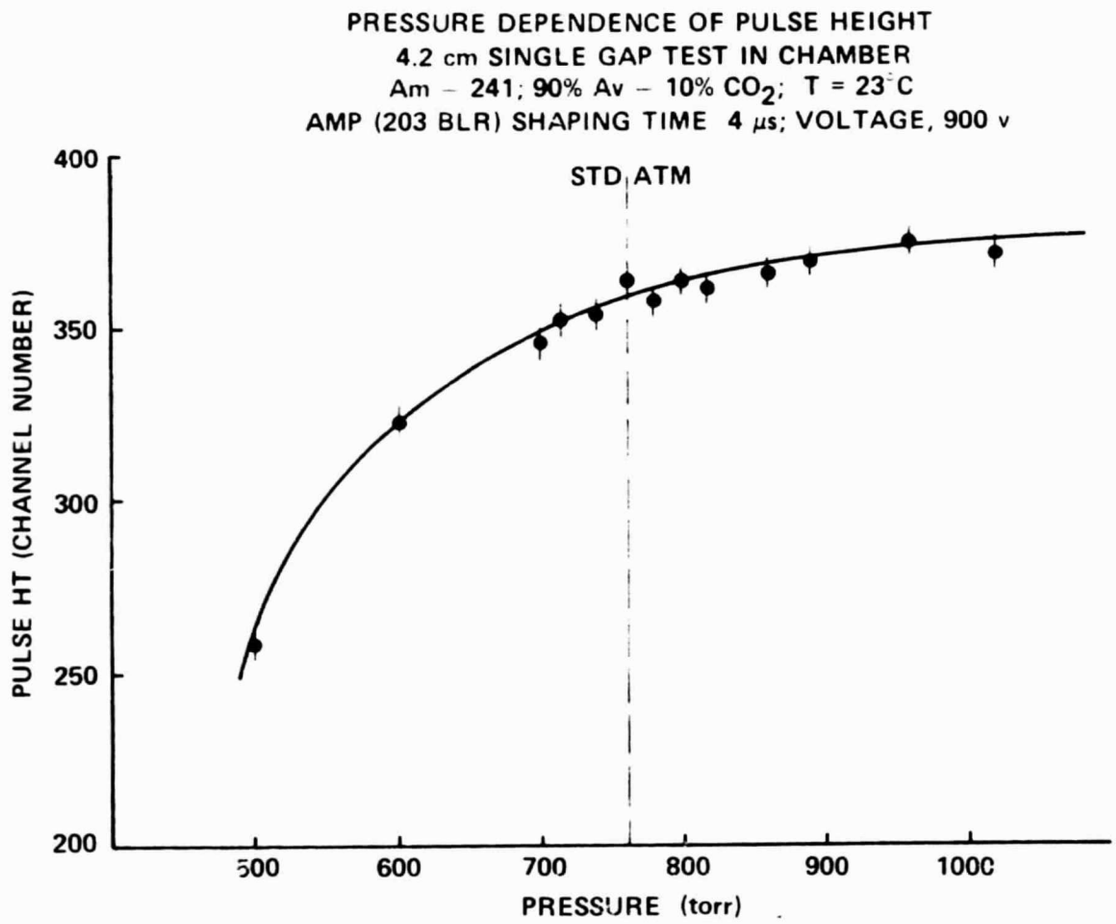
PRESSURE DEPENDENCE OF PULSE HEIGHT
4.2 cm SINGLE GAP TEST IN CHAMBER
Am – 241; 90% Av – 10% CO_2; T = 23°C
AMP (203 BLR) SHAPING TIME 4 μs; VOLTAGE, 900 v
STD ATM
PULSE HT (CHANNEL NUMBER)
400
350
300
250
200
500
600
700
800
900
1000
PRESSURE (torr)

FIGURE 28.

should be emphasised that this experiment is rather specific for the set-up used: 4.2 cm of argon and 5.5 MeV α-particles; however, it may be deduced that there should be no difficulty in this respect with minimum ionizing particles.

Electronics

Detection of charge pulses of the order of 10^{-14} coulomb deposited in large area parallel plate ion chambers with capacitances of several hundred pf requires a very low noise charge-sensitive amplifier. A low power device to meet these requirements has been designed and used successfully on balloon flights. The diagram is shown in Figure 29. The detector (ion chamber anode) is ac-coupled to the FET input allowing the use of a large feedback resistor in the charge loop. The FET must be specially selected for low noise.

The design requirements of good signal/noise ratio at z=6 (carbon) are exceeded by the this amplifier-detector combination. Measured capacitance between anode and cathode in both ion chambers was 260 pf approximately. Rms noise was 7mV measured at the postamplifier output, or about 6300 rms electrons, giving a signal to noise ratio of better than 4:1 at z=3.

A relativistic iron nucleus $_{26}Fe^{56}$ (at 10 GeV per nucleon) deposits about 44 MeV of energy in a normal track through the xenon-filled balloon flight ion chamber. This corresponds to 2.01×10^{6} ion pairs, or 3.21×10^{-13} coulombs of charge of either sign. The amplifier (gain ~ 12) produces a pulse of about 4 V for this charge which corresponds to about channel 400 of the 1024 channel ADC.

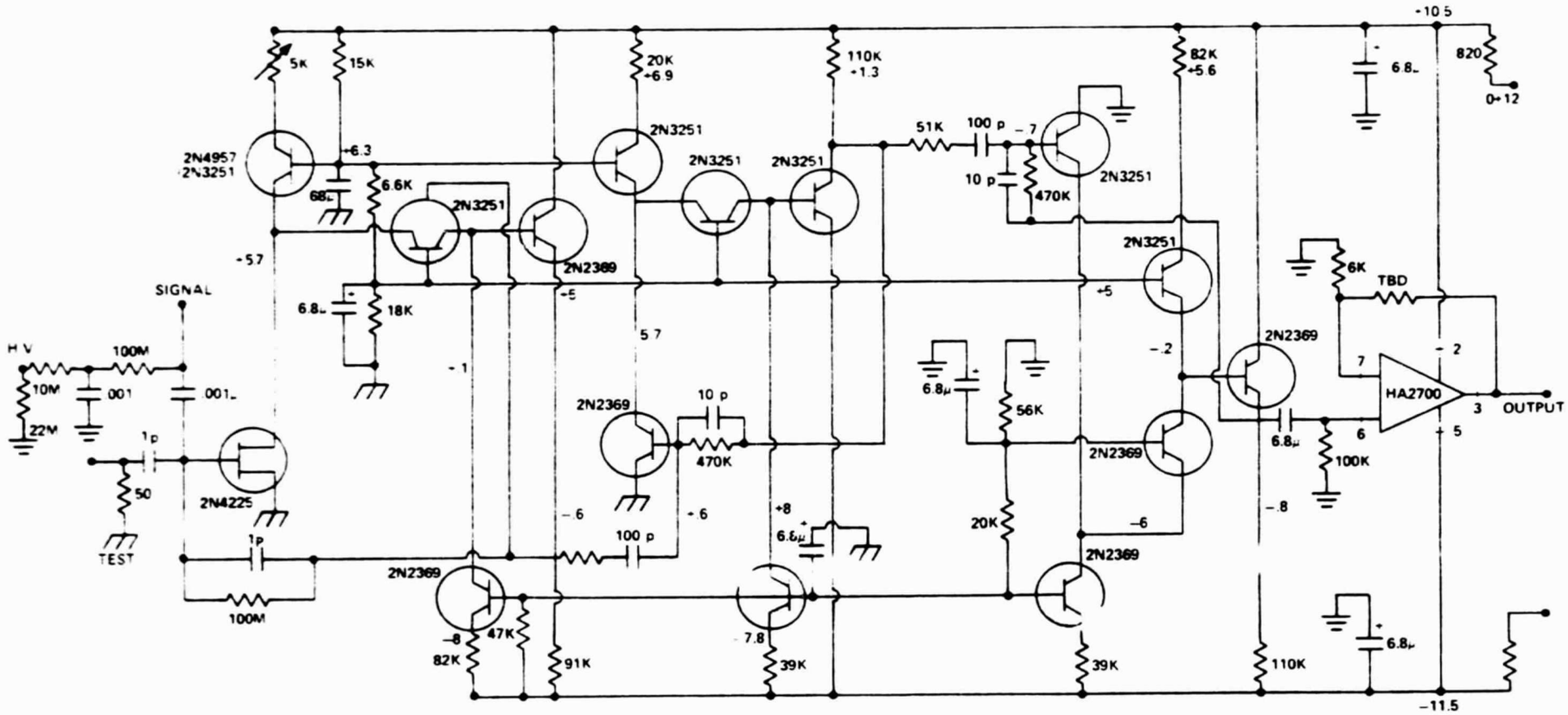

BALLOON ION CHAMBER AMPLIFIER

FIGURE 29.

Calibration

Laboratory and in-flight calibration is made with Am-241 sources of 5.5 MeV α-particles. These have a range of 2.1 cm in xenon at 1 atmosphere and normal temperatures. The foil-supported sources are mounted in the center of the cathode screens on the outside of the gap, one to each flight chamber. These are uncollimated in the present version. The source in the cylindrical test ion chamber is collimated producing a much narrower pulse-size distribution. An example of the effect of collimation on this distribution is given for some collimators. In each case the foil source is placed behind a hole or holes drilled through the 1/8 in. thick aluminum cathode disc. The collimating holes were:

1) 1/8 in. diameter hole, 1/8 in. long (45^{o} spread)
2) 1/16 in. diameter hole, 1/8 in. long (26.5^{o} spread)
3) 35 holes 1/32 in. diameter, 1/16 in. long over circle 1/4 in. diameter (26.5^{o} spread)

The variations of pulse height distribution is given for these three cases in terms of the FWHM; 1) 15.6%, 2) 6.4%, 3) 6.6%. The peak of the pulse distribution fell at channel 339 for case; 1) compared to channel 314 for case; 2) and the tail on the higher charge side of the distribution extended further in case 1).

This result indicates that the charge deposit from Am-241 in our configuration is not strictly comparable in terms of pulse height with a charge deposit from a relativistic particle. However, such an absolute calibration is not necessary.

2-93-58

N77-25049

SCINTILLATING PLASTIC FIBERS AS LIGHT PIPES FOR A COSMIC RAY HODOSCOPE:

Feasibility calculations and measured attenuation characteristics.

1. Objectives of this Study

Some cosmic ray experiments of the next decade will attempt to measure abundances in the high z portion of the charge spectrum where fluxes may be few particles m^{-2} sr^{-1} yr^{-1}. Such experiments require large areas to obtain adequate exposure and thus the development of charged particle hodoscopes of several square meters is needed.

A candidate hodoscope would use arrays of scintillator fibres, followed by an image intensifier and imaging system such as that proposed for the x-ray shadowgraph (Ref. 1). A literature search was performed to ascertain the experience of other workers with hodoscopes using this or similar principles. Calculations were performed to determine the feasibility of candidate systems and some laboratory experiments were performed to attempt to check these numbers.

2. Plastic Scintillator Properties

The properties of NE 102 fibres which make them interesting for our application are (a) their scintillating property, (b) their uniformity, (c) their availability in long lengths of various diameters, (d) their light guiding properties, (e) their low absorption coefficient for their own scintillation light and (f) the possibility of obtaining clad fibres.

The plastic scintillating fibre we are interested in this article is NE 102 by Nuclear Enterprises, Inc. with the following specification:

Diameter		1.0 mm
Index of Refraction		1.58 (not clad)
Critical Angle of Total Reflection	=	39.2652°
Specific Gravity	=	1.032
Light Produced	=	4230Å (2.9 ev)

3. Energy deposition of different Z number particles and the total number of photons generated in NE 102 fibres

We performed calculations for three different charged particles: minimum ionizing ^{26}Fe and ^{6}C, and α particles from Am^{241} decay. The energy deposition $\frac{dE}{dx}$ of each one in the fibre is 870 Mev/gm for minimum ionizing ^{26}Fe; 46.8 Mev/gm for minimum ionizing ^{6}C; and the α energy is 5 Mev approximately. Only a part of this energy can be converted to photons (4230Å, 2.9 ev) in the plastic scintillating fibres due to the saturation effect and conversion efficiency. The total number of photons (Np) can be calculated by the formula.

$$Np = \frac{E}{Ep} \times \eta \times \eta_{sat}$$

where Np = Number of photons

E = Energy deposition

Ep = Photon energy

η = Conversion efficiency (0.02 in our case)

η_{sat} = Saturation coefficient (0.2 in our case)

The saturation coefficient is a function of dE/dx in the scintillator. If the energy deposit per unit volume exceeds some value, the emission centers no longer respond linearly. For minimum ionizing particles in plastic scintillators, η_{sat} becomes less than one at about Z = 16. It is significantly less than one for stopping α's (~ 0.2). In these calculations η_{sat} is taken as 0.2 for all three particles considered here, and consequently the ^{6}C case is treated rather conservatively.

For α particles in 1 mm thick fibre

$$Np = \frac{5,000,000}{3} \times 0.02 \times 0.2 = 6,700 \text{ photons}$$

For C particles in 1 mm thick fibre

$$Np = \frac{4,680,000}{3} \times 0.02 \times 0.2 = 6,240 \text{ photons}$$

For Fe particle in 1 mm thick fibre

$$Np = \frac{87,000,000}{3} \times 0.02 \times 0.2 = 116,000 \text{ photons}$$

4. Light Guide Properties of Fibres

If the particle-induced photons are evenly distributed in 4π radians inside the fibre, then only a small fraction of these photons inside the total reflection cone can be transmitted by the fibre. This fraction can be calculated as follows:

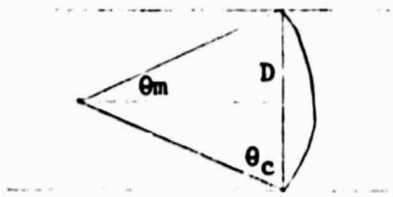

Solid angle of the total reflection cone = $\frac{\int dA}{r^2}$

where $dA = r d\theta \times 2\pi r \times \sin\theta$

$$A = \int dA = \int_{\theta=0}^{\theta=\theta_m} 2\pi r^2 \sin\theta \, d\theta$$

$$= 2\pi r^2 \cos\theta \Big|_{\theta=0}^{\theta=\theta u_m = 90^\circ - 39.2652^\circ}$$

$$= 2\pi r^2 \times (0.3572)$$

The fraction (f)

$$f = \frac{\Omega}{4\pi} = \frac{\frac{A}{r^2}}{4\pi} = \frac{\frac{2\pi r^2 (0.3572)}{r^2}}{4\pi}$$

$$= 0.178$$

That is, if the reflectivity is 100% and the absorption coefficient is zero only 0.178 of the photons can be transmitted to one end. This result is independent of fibre diameter.

For α particle, there will be 6,700 x 1.178 = 1,200 photons which can be transmitted to PM tubes.

For C particle, there will be 6,240 x 0.178 = 1,110 photons which can be transmitted to PM tubes.

For Fe particle, there will be 116,000 x 0.178 = 20,648 photons which can be transmitted to PM tubes.

But the reflectivity and absorption coefficient become important if the guide length is long, (large number of reflections and long optical path).

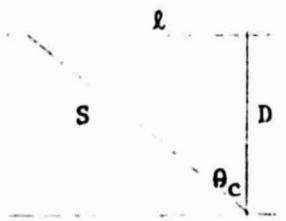

The maximum number of reflections N_R

$$N_R = \frac{L \text{ (total length)}}{\ell} = \frac{L}{D \tan \theta_c}$$

The maximum optical length S

$$S = \frac{D}{\cos \theta_c} \times N_R = \frac{L}{\sin \theta_c} \text{ (Independent of D)}$$

Table 1 shows the light transmission efficiencies of 1 mm diameter fibres of various lengths. Table 1.1 shows the effect of absorption only: table 1.2 of reflection loss only and 1.e gives the total transmission efficiency using reflectivities obtained from Ref. 2.

Table 2 and 3 convert the light produced by the 3 types of particle to photon numbers and photoelectron numbers, respectively, both quantities refering to the condition at the photo cathode.

TABLE I Total Light Transmission Efficiency for 1 mm Diameter Fibres of Different Kinds

1-1 Transmission Efficiency Due to Absorption

Fibre Length	100cm		50cm		10cm	
Max Optical Length (For Ray at Total Internal Reflection angle)	158cm		79cm		15.8cm	
Absorption Coefficient	$0.015cm^{-1}$	$0.018cm^{-1}$	$0.015cm^{-1}$	$0.018cm^{-1}$	$0.015cm^{-1}$	$0.018cm^{-1}$
Light Left	9.3%	5.8%	30%	24%	79%	75%

1-2 Transmission Efficiency Due to Reflection Loss

Fibre Length	100cm			50cm			10cm		
Max Number of Reflection	1224			612			122		
Reflectivity	99.9%	99.5%	99.3%	99.9%	99.5%	99.3%	99.9%	99.5%	99.3%
Light Left	29.3%	0.2%	0.02%	54%	4.6%	1.3%	88%	54%	42%

1-3 Total Transmission Efficiency [Eff (abs.) x Eff (refl.) x 0.178]

	Reflectivity	Absorption Coefficient	100 cm	50 cm	10 cm
Fibre A*	99.9%	$0.015cm^{-1}$	4.8×10^{-3}	2.9×10^{-2}	1.2×10^{-1}
Fibre B	99.5%	$0.015cm^{-1}$	3.3×10^{-5}	2.5×10^{-3}	7.6×10^{-2}
Fibre C	99.3%	$0.018cm^{-1}$	2.1×10^{-6}	5.5×10^{-4}	5.6×10^{-3}

* Fibre A, very good fibre

Fibre B, good non-clad fibre

Fibre C, regular fibre (Ref. 2)

TABLE 2 Photons reaching PM Tube for Different Sources and Different Fibres

SOURCE	Photon induced	Photon can be transmitted	100 cm			50 cm			10 cm		
			Fibre A*	Fibre B*	Fibre C*	Fibre A	B	C	A	B	C
α	6,700	1,200	32	0.22	1.37×10^{-2}	1.94×10^{2}	16.3	3.56	8.1×10^{2}	4.9×10^{2}	3.56×10^{2}
C	6,240	1,110	30	0.20	1.3×10^{-2}	1.79×10^{2}	15.3	3.46	7.7×10^{2}	4.7×10^{2}	3.49×10^{2}
Fe	1.16×10^{5}	20,648	5.6×10^{2}	3.8	0.23	3.2×10^{3}	2.8×10^{2}	6.4×10^{2}	1.4×10^{4}	8.7×10^{3}	6.4×10^{3}

* See foot note on Table 1-3

REPRODUCIBILITY OF THE ORIGINAL PAGE IS POOR

TABLE 3 Photoelectrons produced at photocathode

SOURCE	100 cm			50 cm			10 cm		
	Fibre A	B	C	A	B	C	A	B	C
α	3.2	0.22×10^{-1}	1.37×10^{-3}	1.94×10^{1}	1.63	0.36	8.1×10^{1}	4.9×10^{1}	3.56×10^{1}
C	3.0	0.2×10^{-1}	1.3×10^{-3}	1.79×10^{1}	1.5	0.3	7.7×10^{1}	4.7×10^{1}	3.49×10^{1}
Fe	5.6×10	0.4	0.2×10^{-1}	3.2×10^{2}	2.8×10^{1}	6.4	1.4×10^{3}	8.7×10^{2}	6.4×10^{2}

5. Quantum Efficiency and Background of PM Tube

Table 3 shows the number of photoelectrons induced for different fibres and different sources at different distances. A typical photocathode quantum efficiency of 10% was employed.

A typical photocathode may emit 5,000/sec,cm^2 thermionic electrons at room temperature. This is the main portion of the background. In our experiment we applied a 1½ inch PM tube (≈ 11 cm^2 in surface area), which will emit about 55,000 electrons at room temperature. There would be ~ 55 output pulses/sec (0.1% of the 55,000 electrons) (Ref 3,4) with pulse heights corresponding to at least the average height for nine electrons starting at the photocathode.

This means that for expected count rates, events could not be observed which produced only 9 photoelectrons (90 photons at photocathode). The crossed area in Table 3 showed difficulty of observation. But it should be quite possible to observe high Z particles over a 50 cm length with any one of the fibres on Table 3.

6. Experimental Results

In the laboratory, we attempted to obtain Am^{241} α spectra within 50 cm using NE 102 plastic scintillating fibre (Nuclear Enterprises, Inc.) in the arrangement shown in Figure 1. According to the manufacturer's report, the light loss of NE 102 is only about 0.009/cm corresponding to an attenuation length 2.5m. But unfortunately, we cannot observe any further than 2 inches (Figures 2, 3, 4, 5, 6). The ends of the fibres were cut and polished and epoxied to microcope cover glasses. These in turn were coupled to the PM tube with coupling compound.

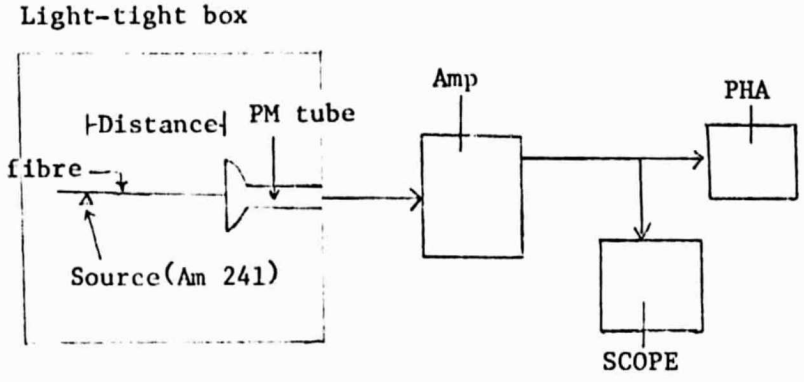

Figure 1 The Experiment Set-up

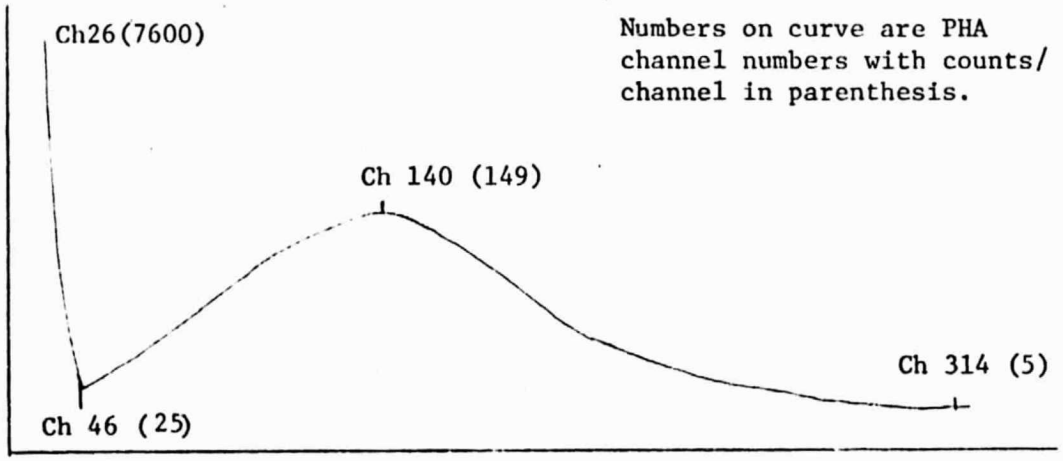

Figure 2 Am 241 Source right on the PM tube.
Accumulation time 450 Sec.

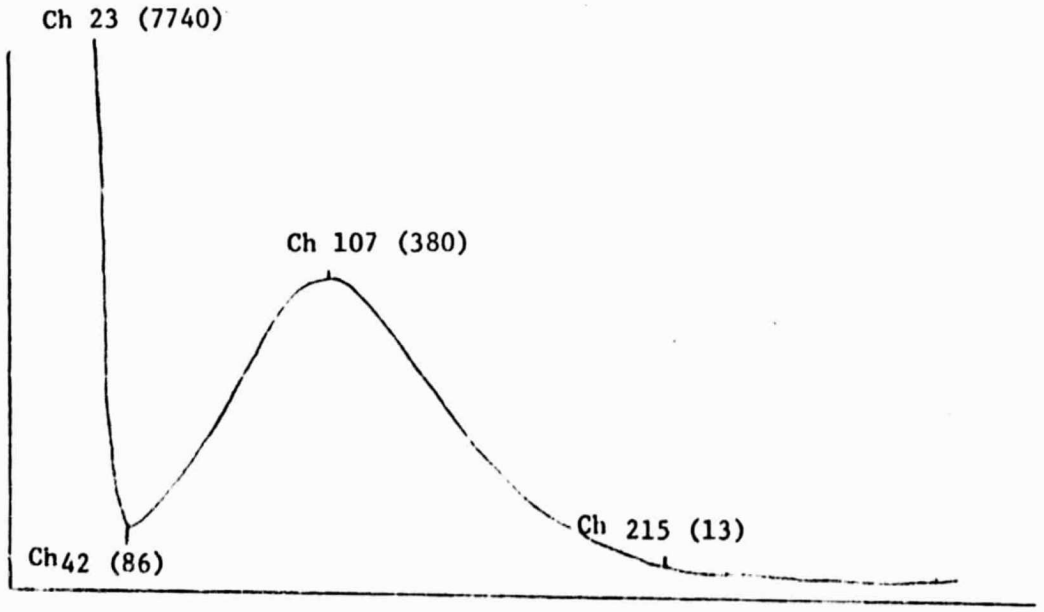

Figure 3 Am 241 Source 0.5" away from PM tube

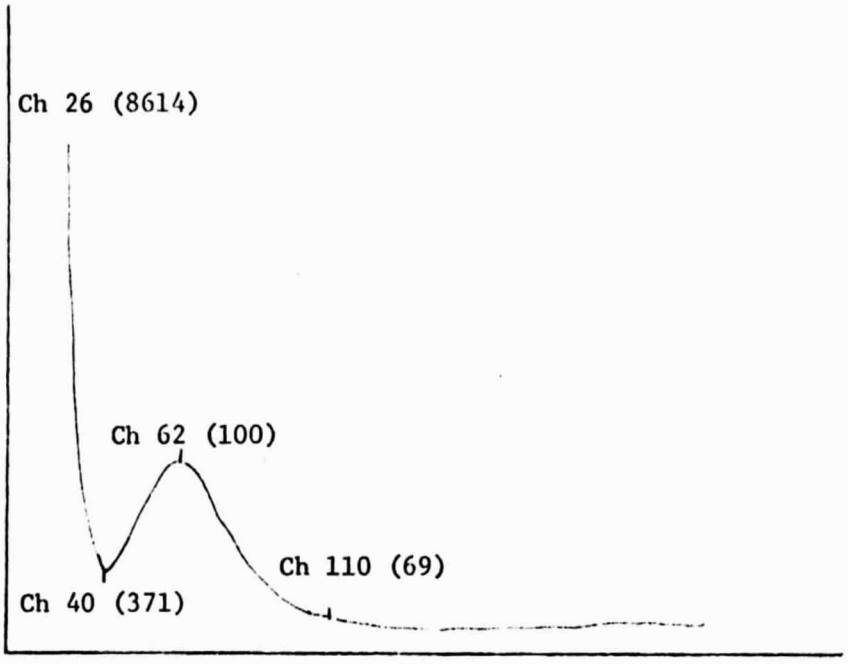

Figure 4 Am 241 Source 1" away from PM tube.

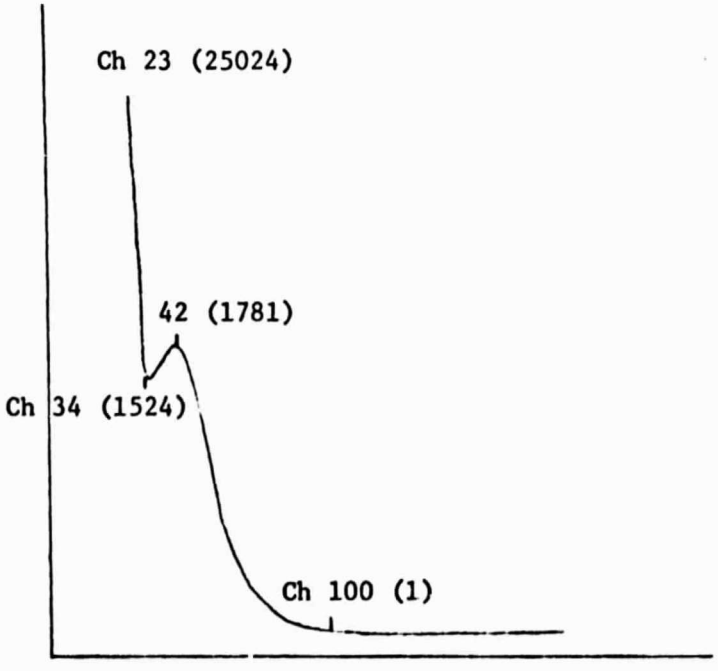

Figure 5 Am 241 Source 4 cm away from PM tube.

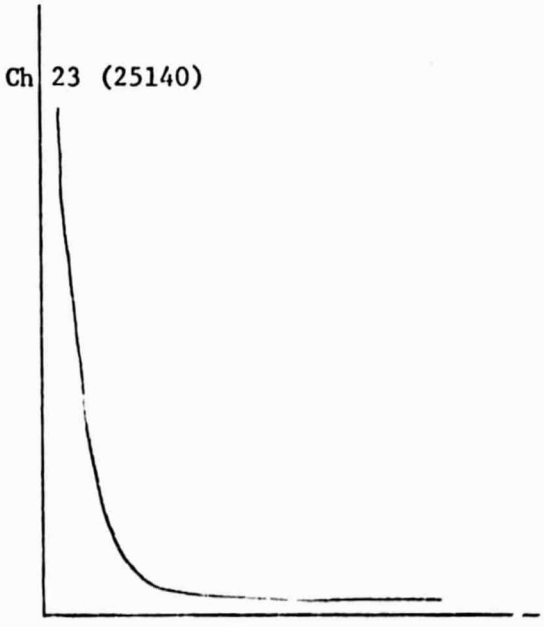

Figure 6 Am 241 Source 5.5 cm away from PM tube.

Figure 2 shows Am^{241} α-counts up to channel 314 on the PHA with a photoelectron noise spectrum cut off at about channel 46. If this latter corresponds to ~ 9 photoelectrons, a pulse in channel 314 corresponds to ~ 63 photoelectrons. We calculated that roughly 120 photoelectrons should be produced under these experimental conditions; an estimate well within limits of error caused by uncertainty in the numerical values used.

It is thought that surface damage such as scratch as, cracks, attached dirt, etc., perhaps produced by bad handling or bad end-cutting, was having a critical effect on the reflection efficiency, resulting in the loss of most photons within a gas centimeters.

TABLE 4 Shows if the reflectivity dropped down to 95%, very few photoelectrons will be produced.

SOURCE	Reflectivity	Light left after 5 cm	Photons on PMT	Photoelectrons
α	90%	0.16% x0.178 = 0.028%	1.94	0.192
α	95%	4.3% x 0.178 = 0.765%	52	5.2
α	96%	8.2% x 0.178 = 1.46%	99.4	9.9
α	97%	15.6% x 0.178 = 2.78%	187	18.7

TABLE 4

Fibure 7 is a plot of relative light intensity vs. distance. From the relation $I = I_o \rho^N$ (where ρ is the reflectivity and N the number of reflection we estimated that the reflectivity (ρ) for 2 different fibres was 95-97%. From Table 4, we see that for an αparticle interacting with the fibre 5 cm from the photomultiplier tube, only 5-19 photoelectrons are produced at the photocathode. This is of the same magnitude as the tail of the thermal noise spectrum.

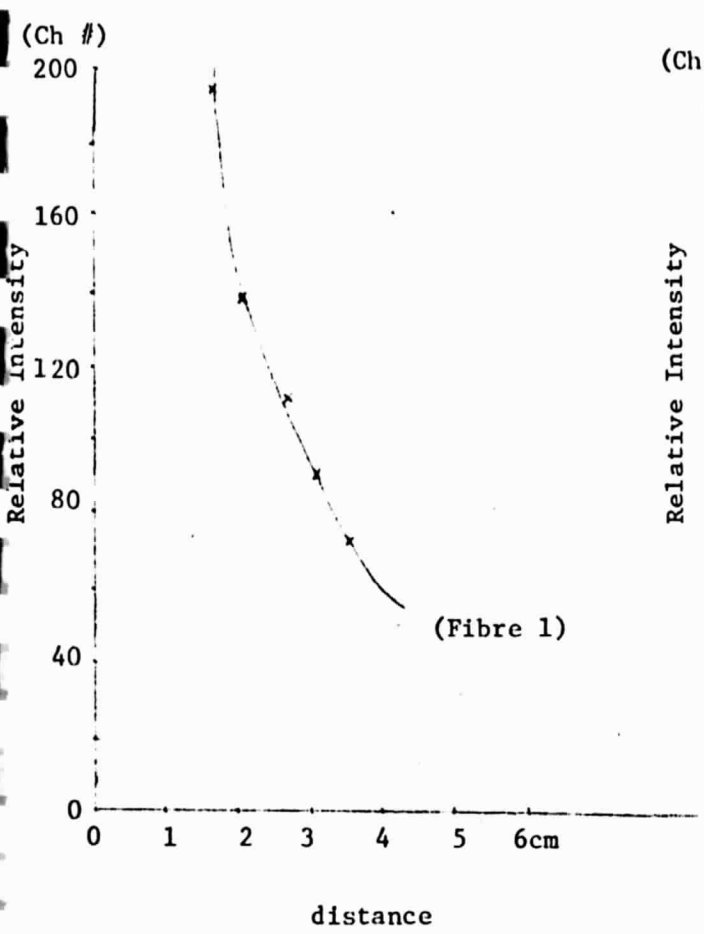
(Ch #)
200
160
120
80
40
0
Relative Intensity
(Fibre 1)
0 1 2 3 4 5 6cm
distance

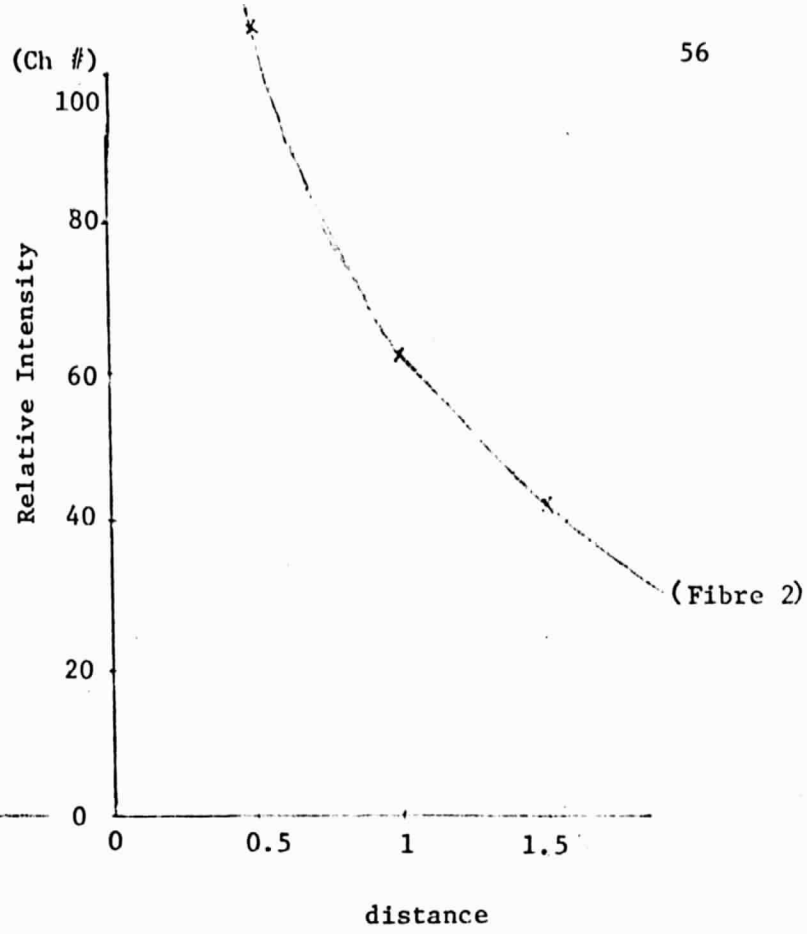
(Ch #)
100
80
60
40
20
0
Relative Intensity
(Fibre 2)
0 0.5 1 1.5
distance

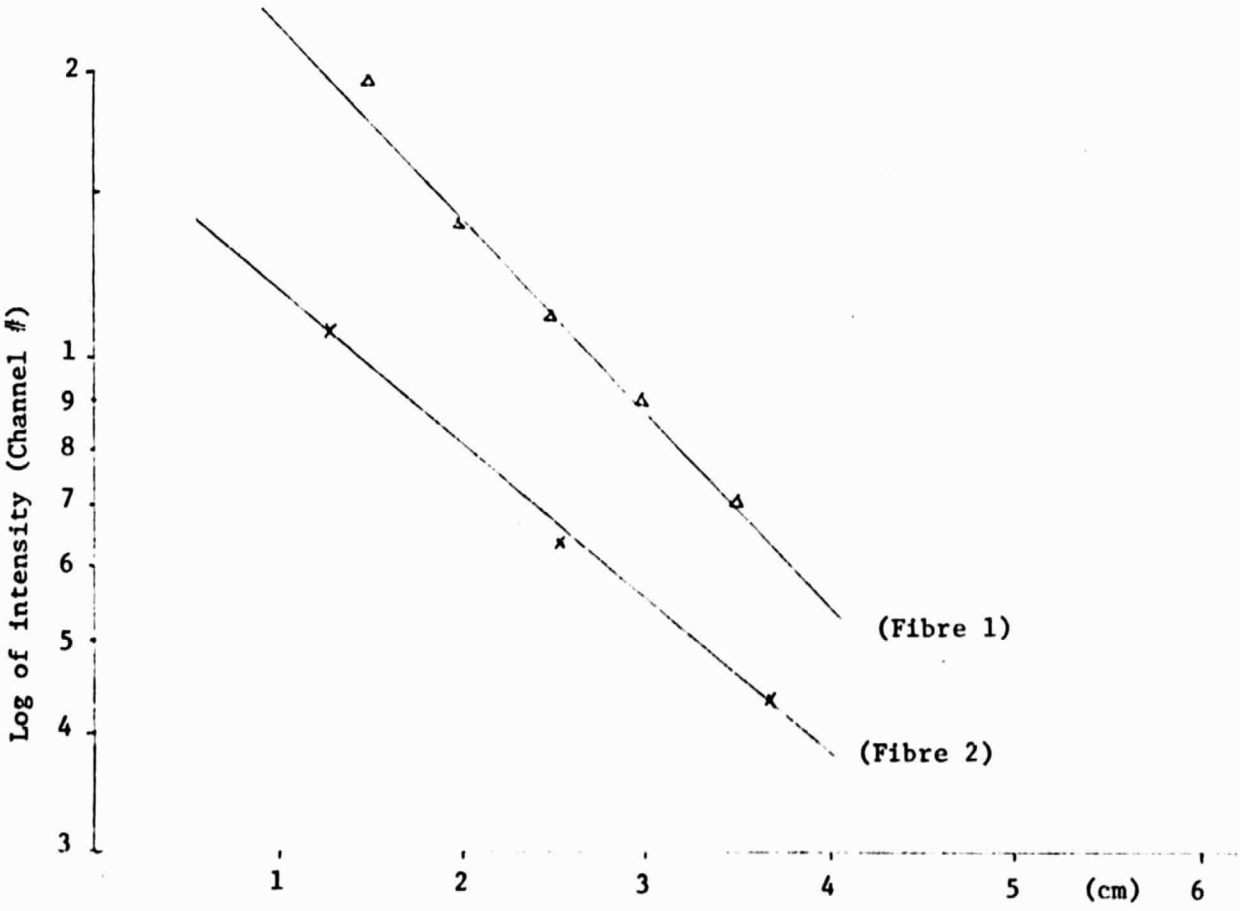
Log of Intensity (Channel #)
2
1
9
8
7
6
5
4
3
(Fibre 1)
(Fibre 2)
1 2 3 4 5 (cm) 6

(Figure 7)

7. Conclusions

Plastic fibre scintillators 5 x 5 x 5 cm^3 have been used (Ref. 10) as beam finders for 700 MeV protons but no reports have been found of much longer hodoscopes. Other systems are described in Ref. 11 by Reynolds and coworkers (Princeton), Caldwell and coworkers (MIT), and an Imperial College, London, group.

Glass fibres tend to have and maintain better surface smoothnes and Flanagan et al. (Ref. 11) report detectability of Z=1 minimum ionizing particles at 20-25 cm. in 1 mm. diameter glass fibres. Experimental details were not given. They are not readily obtainable in long lengths (> 20 cm.).

Recent progress on optical fibre transmission line techniques (Ref. 5), can reduce the surface damage produced by cutting to the minimum. Gloge, Smith, Bisbee et al. at Bell Laboratories presented a method and their special tool to cut and connect fibres with little loss (Ref. 6, 7, 8, 9).

Experimental results given here agreed well with calculated values of the photomultiplier-plastic scintillator output for Americium - 241 α-particles. The fibres used in the laboratory were found to have internal reflectivities (95-97%) lower than the range of those reported in the literature probably because we took no special precautions in handling them. It was demonstrated that, for fibres of the lengths of interest for a charged particle hodoscope, reflection losses are dominant.

Tabel 3 shows that for a 1 m. transmission length a reflectivity of 99.9% is required. This is difficult (but not impossible) with unclad fibres but not difficult with clad fibres. Thus, with good quality fibres, transmission distances of over 1 m. should be readily obtained.

Further measurements should be made with clad plastic fibres and glass fibres.

8. References

1. G. J. Fishman, T. A. Parnell, T. A. Rygg, J. C. Gregory, An X-ray Shadowgraph to Locate Transient High Energy Celestial Sources. Presented at the Symposium on Charged-Coupled Image Device Technology for Scientific Image Applications, JPL March 6-7, 1975.

2. Potter, Transmission Properties of Optical Fibres, Journal of OSA 51, 1960.

3. Price, Nuclear Radiation Detection, p. 192, 1964.

4. G. A. Morton, J. A. Mitchell, Nucleonics, 4:16 (January 1949).

5. 1975 Optical Fibre Transmission Technical Digest. (OSA)

6. J. Stone, Low-Loss Splices in Optical Fibres, Bell Systems Technical Journal, Vol. 52, No. 7, Sep 1973.

7. C. G. Someda, Simple, Low-Loss Joints in Optical Fibre BSTJ Vol. 52, No. 4, April 1973.

8. D. L. Bisbee, Optical Fibre Joining Technique, BSTJ Vol. 50, No. 10, December 1971.

9. Gloge, P. W. Smith, et al. Optical Fibre End Preparation for Low-Loss Splices, BSTJ, Vol. 52, No.

10. Lisitsa, Fibre Optics, p. 238, 1972.

11. Photoelectronic Image Devices. Proceedings of the Second Symposium held at Imperial College. Ed. McGee, Wilcock & Mandel, Academic Press, N. Y. (1962).

3-73-63

N77-25050

EVALUATION OF CLAD SCINTILLATING LIGHT PIPES

INTRODUCTION

Arrays of fibers made of scintillating material have been used as position-sensitive detectors or hodoscopes for beam-finding at ion accelerators. Under this contract we have previously evaluated unclad fibers of NE 102 (Nuclear Enterprises, San Carlos) for use in a hodoscope for a heavy cosmic ray experiment. Experiments were made with α's from an Am^{241} source incident upon one end of the fibre, the other end being viewed with a photomultiplier tube. The scintillation light could not be detected in any of the fibers tested beyond about 5 cm. These previous results and calculations of the effective useful lengths for detection of relativistic heavy ions were given in a report and are reproduced in this Final Report.

Light transmitted down a transparent fiber suffers a maximum of $N = \frac{1}{2r \tan \theta_c}$ reflections per cm, where r is the radius of the fiber and n the index of refraction of the material $\left(\theta_c = \arcsin \frac{1}{n}\right)$ The transmission of a length L of the fiber, assuming it is optically clear, is given by $t = \alpha^{NL}$ where α is the reflection efficiency. This expression shows that the transmission of such fibers depends very sensitively on the reflection coefficient, which in turn is a function of the surface condition of the fiber. This finish is dependent on the manufacturing process and how the material is handled afterwards, conditions which are very difficult to measure and control. To obviate this problem fibers may be coated or clad with another material of lesser refractive index which serves to protect the surface

of the fiber. The attendant light loss caused by the reduction of solid angle included in the cone of total reflectance is usually negligible when compared to the gains from increase in reflectivity at the fiber/cladding interface. Transmission lengths of miles are now reported for clad glass light pipes. However, the change from an air/PVT interface (θ_c = 39°) to a plexiglass/PVT interface (θ_c = 71°) results in a drop in solid angle content of the cone of permitted light transmission from about 18% to 3% for undirected light. This factor is independent of the fiber radius.

Since no clad fibres of scintillating material were available commercially, we have fabricated some and tested them using the same method as before.

Fiber Manufacture

Two scintillator materials were obtained from Nuclear Enterprises, NE 102 and NE 150. The first is a polyvinyltoluene matrix and the second polystyrene. Each contained a proprietary and undisclosed mixture of scintillation chemicals. NE 102 has a claimed conversion efficiency of about 2% while NE 150 (no longer available) is less efficient. The materials were crushed from block form into particles which would pass a 0.25 inch sieve by Gold Plastics of Los Angeles.

The granulated material was heated and extruded into a polymethylmethacrylate (plexiglass) sleeve which comprised the billet from which the fibers were drawn. Fiber manufacture was performed by International Fiber Optics of San Diego.

The following amounts of material were received:

Fiber Core Material	Nominal Diameter (inches)	Length (ft.)
NE 150	0.04	75
NE 150	0.06	150
NE 102	0.04	200
NE 102	0.06	120
NE 102	0.08	100

Geometrical Characteristics of Clad Fibers

Geometrical measurements are made on a fifteen-foot sample of each type of fiber. A wide variety of imperfections were noted but we are not able to discriminate between different types or magnitudes of imperfection in terms of quantitative effect on light transmission. Typical diameters measured are given below.

	TYPE OF FIBER	TYPICAL DIAMETERS (IN.)
1.	NE 150 .04"	Major Axis .033 Minor Axis .034
2.	NE 150 .06"	Circular .061
3.	NE 102 .04"	Major Axis .034 Minor Axis .030
4.	NE 102 .06"	Major Axis .051 Minor Axis .035
5.	NE 102 .08"	Major Axis .076 Minor Axis .073

Other Imperfections:

1. Uniform except for knots up to 0.06 inch diameter every few feet.
2. Very circular but occasional large knots up to 0.11 inch diameter.

3. Slight flattening but no major faults visible.

4. Pitted surface.

5. Not smoothly circular or elliptical like most of the fibers. Ridges present where fibers apparently stuck to each other after forming.

Optical Characteristics

The optical characteristics of the NE 150 fibers were so poor as to render them useless. For the plexiglass-clad NE 102 fibers we have:

$N_{102} = 1.58$

$N_{pl.} = 1.49$

$\theta_c = 70.6°$ (Critical angle for combination)

$\lambda_{scint.} = 4230\text{Å}$ (Peak of scintillation spectrum)

Fibers were cut and polished and placed in a dark box with one end grease-coupled to a 2 inch photomultiplier and the other close to a source of α particles $\left(Am^{241}\right)$. Lengths used were the longest for which these signals could be observed.

The largest (0.080 inch) diameter fiber showed the best performance but even this was not very good. The maximum distance at which an Am^{241} α-produced scintillation could be observed using the same experimental arrangement given previously was between 5 and 6 inches. Previous best transmitted distance with the unclad fibers was about 2 inches though this was with a fiber of half the diameter (1mm).

A plot of logarithum of the transmitted intensity (t) versus transmitted distance (figure 8) shows from the relation

$$I = I_o \rho^{NL} \qquad (t = I/I_o)$$

a value of 92-95% for the reflectivity.

This is no better than that found for the unclad fibers but an important uncertainty exists in the value of N. We have used the maximum value of reflections (i.e. those at the total internal reflection angle, through the mean number of reflections suffered by a photon will be less).

Conclusion

Specially manufactured clad scintillating plastic fibers were tested in the laboratory and found to be of poor quality. Only a small improvement of a factor of 2 in transmission was achieved by cladding in this instance. Much better fibers could doubtless be produced but this would require our spending much effort in fiber manufacturing technology.

LOCATION OF TRANSIENT GAMMA-RAY SOURCES WITH THIN FLAT SCINTILLATORS

T. A. Parnell

Space Sciences Laboratory, NASA
Marshall Space Flight Center, Huntsville, Alabama 35812

and

J. C. Gregory and T. L. Kuo

The University of Alabama in Huntsville
P. O. Box 1247
Huntsville, Alabama 35807

IEEE Transactions on Nuclear Science, Vol.NS-23, No.1, February 1976

LOCATION OF TRANSIENT GAMMA-RAY SOURCES WITH THIN FLAT SCINTILLATORS

T. A. Parnell,

Space Sciences Laboratory, NASA,
Marshall Space Flight Center, Huntsville, Alabama 35812

and

J. C. Gregory and T. L. Kuo

The University of Alabama in Huntsville
P. O. Box 1247
Huntsville, Alabama 35807

Summary

Thin flat slabs of scintillator are a useful means of measuring angular location of gamma-ray fluxes of astronomical interest. A statistical estimate of position error has been made of two scintillator systems suitable for gamma-ray burst location from a balloon or satellite platform. A single rotating scintillator with associated flux monitor is compared with a pair of stationary orthogonal scintillators. Position error for a strong burst is of the order of a few arcmin if systematic errors are ignored.

Introduction

Slabs of scintillator may be used as directional gamma ray detectors for a number of studies in astronomy including measurement of cosmological gamma ray anisotropy, location of discrete sources, measurement of atmospheric anisotropy, and location of gamma ray bursts.

We examine here only the last of these, and attempt to estimate the position error of scintillator systems of reasonable dimensions used to locate these transient phenomena.

Five years ago the gamma ray bursts were discovered by detectors on Vela spacecraft. Since then some 40 bursts have been detected by at least 9 spacecraft in addition to several Vela satellites. The bursts are a unique phenomenon with no parallels in other energy regions or time scales of astronomy. Compared to other astronomical sources of gamma rays the bursts have large flux, a hard spectrum and duration of less than one second to some tens of seconds. They have not yet been identified with any optical or x-ray object. Crude position measurements with uncertainties of 5°-10° are available for less than a dozen bursts and so far indicate an apparently random distribution.

The next major step in the understanding of these extremely energetic processes requires their position location to a degree of accuracy which allows identification with an object previously observed in some other spectral region. Candidate instruments and techniques which have been proposed for this purpose, include long baseline timing,[1] the x-ray shadowgraph,[2] an array of one dimensional Dicke cameras,[3] and an active anti-collimator.[4] We examine here an alternative experimental arrangement using the directional sensitivity exhibited by a thin flat scintillator to a parallel beam of gamma rays. The general case of response of such shaped scintillators has been treated in detail by a number of authors, most recently Trombka et. al.[5] (1975). We have selected here a scintillator of dimensions suited to the purpose of locating the direction of the gamma ray bursts from a small satellite.

We have examined two configurations in detail. The first consists of a planar scintillator rotating rapidly about an axis in its own plane. A single rotating scintillator would locate gamma ray bursts on an arc. Because of the rapid temporal variability of the burst flux, a second stationary scintillator is required to normalize the flux. The second configuration considered is an orthogonal pair of stationary scintillators of similar dimensions. Both two-detector systems give a line position and require a third scintillator to obtain a point position for the burst origin.

A thin flat detector rotating about an axis perpendicular to the flux vector will respond to that flux according to a rectified cosine function, $|\cos\theta|$. If the position of the flux source is not known the function may be fitted to obtain the offset of the source from some reference direction. We have performed this fitting for some simulated bursts allowing for (a) counting statistics of the quantized flux (b) high local and diffuse background (c) intense variation in flux with time over very short periods.

Photon count rates in the detectors were estimated from published burst spectra[6] and from natural background and used to estimate the location position resolution for various burst strengths. This reslution was compared with that obtained by fixed orthogonal detectors of similar size.

Rotating Scintillator

For a thin flat scintillator of arbitrary shape, area A cm^2 and thickness d cm, the number of counts registered is given by

$$N(E,\theta,t) = \iiint A|\cos\theta|\{1-\exp(-\alpha(E)d\sec\theta)\} \cdot I(E,t)dE\,d\theta\,dt \quad \ldots(1),$$

where θ is the angle between the flux direction and the detect r slab-normal, I is the flux intensity in photons cm^{-2} s^{-1} keV^{-1} and α is the absorption coefficient for the detector material. The spin rate was chosen to be 2 revolutions s^{-1} with counts stored in 1024 bins/π radians. Dwell time per angular bin is 0.244 ms. Counts per angular bin are summed throughout the burst, e.g. for a burst length of 20s, the count rate in a particular angular segment is sampled 80 times. Each

Copyright © 1976 by The Institute of Electrical and Electronics Engineers, Inc.
Printed in U.S.A. Annals No. 602NS083

sum of samples for each angular position is stored in one of 1024 bins. A similar set of 1024 sums is stored in a corresponding register for the stationary detector. Thus the i^{th} bin in the register of one detector covers exactly the same set of time periods as the i^{th} bin in the second register.

The burst count SP summed over the burst period for each bin is calculated from equation (1). To each of these is added the mean background $\bar{B}$ for the same period, which has been previously determined. To simulate experimental reality, this set of numbers (SP+B) is randomized according to Poisson statistics and is called SP(R). The same process is performed for the stationary detector using a different set of random numbers to give ST(R).

To remove the effect of temporal variation of burst flux, the normalized flux (AA) is calculated from

$$AA = \frac{SP(R) - \bar{B}}{ST(R) - \bar{B}}$$

AA still retains the form of $|\cos\theta|$, see figure 1, and is fitted to the trial function $K|\cos\theta|$ where K is a constant of normalization (figure 2). The least squares method then gives the burst direction, θ. This was determined ten times using different random number sets and the standard deviation of θ determined for several burst strengths.

Calculations were performed for a 23 cm x 23 cm x 1 cm CsI(Tl) crystal at a representative energy of 100 keV. In practice a 1 cm CsI slab is rather efficient at this energy and the deviation from the cosine function is not great. Edge effects were ignored.

Several burst strengths were tried and the results of this least-squares fit is shown in Table 1. The strongest bursts have a total energy of $\sim 4 \times 10^{-4}$ erg cm^{-2} and a total of ~400 photons cm^{-2} burst^{-1} in the energy interval 40-200 keV are received at the Earth. The burst time profile of the April 27, 1972 burst as recorded[7] by the Apollo 16, shown in figure 3, was used as a model and the count rates scaled up or down as required.

A total estimated background count of 1 photon cm^{-2} sec^{-1} between 40 and 200 keV for the local (albedo plus charged-particle-produced) and diffuse components was used. This is assumed isotropic and interacts with both front and back surfaces of the detector. This flux is typical for a low inclination, low altitude orbit.

Stationary Scintillator Pair

Consider the response of two stationary orthogonal thin flat scintillators to a γ-ray flux from a direction perpendicular to the line of intersection of their planes. If θ is the angle between the flux vector and the normal to one of the scintillators,

$$\theta = \tan^{-1}\frac{N_2}{N_1} = \tan^{-1}\frac{R_2-B_2}{R_1-B_1},$$

where R_1 and R_2 are the actual count rates measured for each scintillator, and $N_{1,2}$ and $B_{1,2}$ are the respective numbers of burst and background photons respectively for each detector.

The statistical error in θ, measured over part or all of the burst is given by

$$\sigma^2(\theta) = \left(\frac{1}{N_1^2+N_2^2}\right)^2 \left[N_1^2\sigma_{R_2}^2 + N_1^2\sigma_{B_2}^2 + N_2^2\sigma_{R_1}^2 + N_2^2\sigma_{B_1}^2\right].$$

The position error was calculated for the same burst parameters used for the rotating system and is shown in the table. Two cases were considered for each burst type; the burst flux vector in the plane of one detector, and the flux vector at 45° to both detectors.

Conclusion

The estimates of angular position errors made here indicate that the location uncertainties for gamma-ray bursts could be as low as a few minutes of arc for strong bursts and the sizes of scintillators considered if systematic errors in measured rates can be kept below statistical errors. It is noted that statistical errors fall below 1% for the "medium" bursts and these sizes of detector. With respect to systematic errors, the rotating scintillator will have an advantage over two stationary planar detectors. A direct comparison of two detector responses and efficiencies is required for the two fixed scintillators whereas for the rotating scintillator a comparison is only required to correct for temporal fluctuations in the burst flux.

References

1) Giacconi, R., Ap.J., 173, L79, (1972).

2) Fishman G. J., T. A. Parnell, J. C. Gregory, T. A. Rygg, Proc. of Symposium on Charge-Coupled Device Technology for Scientific Imaging Applications, JPL SP-43-21 p4., June 15, 1975.

3) Gorenstein, P., H. Helmken, and H. Gursky, Paper A.5.1, COSPAR/IAU Symposium on Fast Transients in X- and γ-Rays, Varna, Bulgaria, May 1975.

4) Morfill, G. and G. Pieper, Proc. of Conference on Transient Cosmic Gamma- and X-Ray Sources, LA-5505-C, I.B. Strong, Ed., p. 206, (1974).

5) Trombka J. I., J. I. Vette, F. W. Stecker, E. L. Eller, W. T. Wildes, Nucl. Instr. and Methods 117, 99, (1974)

6) Wheaton, W. A., M. P. Ulmer, W. A. Baitty, D. W. Datlowe, M. J. Elcan, L. E. Peterson, R. W. Klebesadel, I.B. Strong, T. L. Cline and U. D. Desai, Ap.J. 185; L57, (1973).

7) Metzger, A. E., R. M. Parker, D. Gilman, L. E. Peterson, J. I. Trombka, Ap.J., 194; L19, (1974).

TABLE 1

Burst Strengths and Angular Resolution

Burst Size	Energy (erg cm^{-2})	Total Burst photons cm^{-2} (40-200 keV)	Burst Duration (s)	$\sigma(\rho)$ (arc min) Rotating Slab	$\sigma(\theta)$ (arc min) Orthogonal Slabs	
					0°/90°	45°/45°
Strong	4×10^{-4}	400	20	6.0	3.3	6.9
Medium	5×10^{-5}	50	7	19.0	16.2	24.5
Weak	5×10^{-6}	5	1	1.5 deg.	1.0 deg.	2.0 deg.

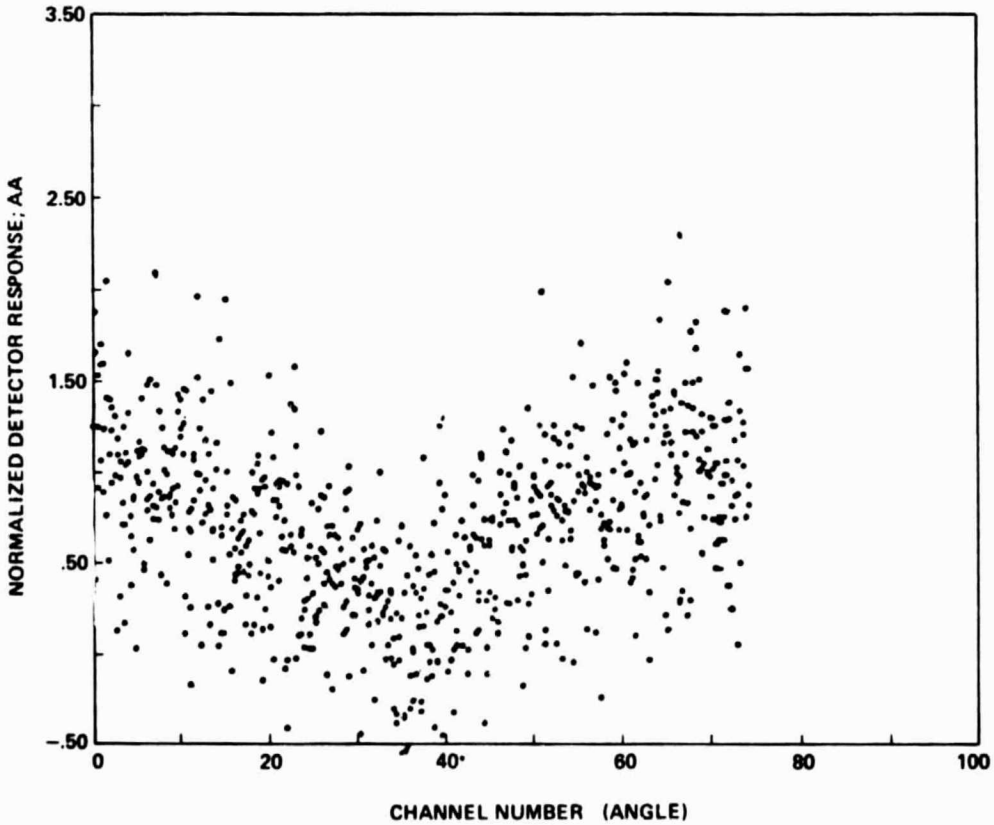

Figure 1. Rotating Detector Response Normalized for Temporal Flux Variations, $AA = \frac{SP(R)-B}{ST(R)-B}$, as a Function of Angle

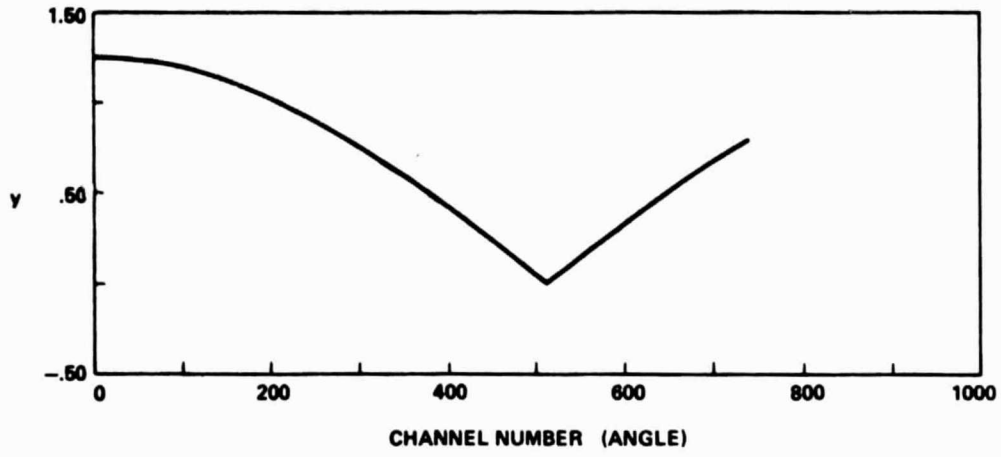

Figure 2. Trial Function, $y = K|\cos\theta|$

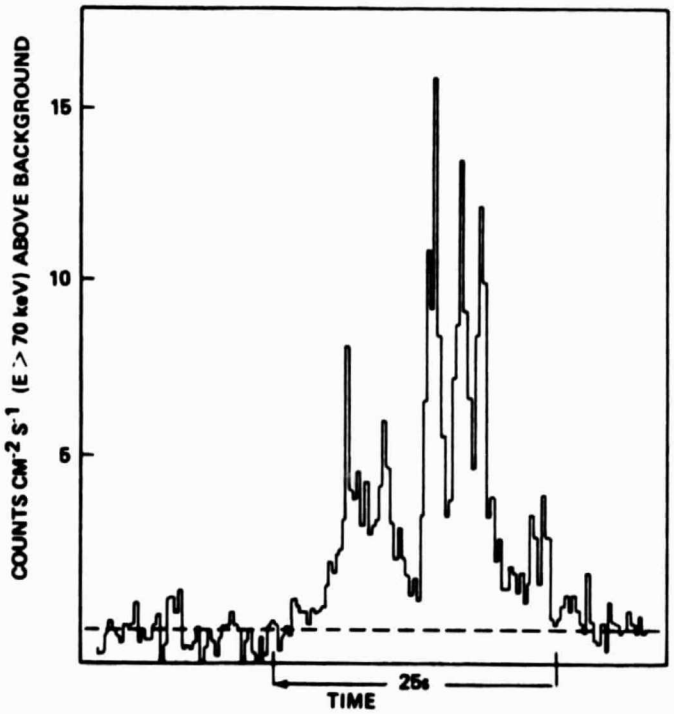

Figure 3. Time Profile of the Gamma-Ray Burst of April 27, 1972, (Metzger et. al.[7]).

Paper by G. J. Fishman, T. A. Parnell, J. C. Gregory and T. A. Rygg Published in the

JPL SP 43-21

PROCEEDINGS

SYMPOSIUM ON CHARGE-COUPLED DEVICE TECHNOLOGY FOR SCIENTIFIC IMAGING APPLICATIONS

March 6-7, 1975

Jet Propulsion Laboratory
California Institute of Technology
Pasadena, California 91103

June 15, 1975

Sponsored by
NASA Office of Aeronautics and Space Technology and
Jet Propulsion Laboratory

AN X-RAY SHADOWGRAPH TO LOCATE TRANSIENT HIGH-ENERGY CELESTIAL SOURCES

G. J. Fishman and T. A. Parnell
Space Sciences Laboratory
NASA/Marshall Space Flight Center
Huntsville, Alabama

T. A. Rygg* and J. C. Gregory
University of Alabama
Huntsville, Alabama

A new technique has been developed to locate strong, transient x-ray sources such as the recently discovered gamma-ray bursts. The instrument, termed a "shadowgraph," locates sources by detecting the x-ray shadow cast by a large occulting mask pattern on an imaging detector. Angular resolutions of from 2 to 10 arc minutes are obtainable while essentially full sky coverage is maintained. The optimum energy range of operation is between 20 keV and 100 keV.

The high-efficiency x-ray imaging detectors, which make it possible to locate bursts with intensities down to ~10 photons/cm^2-sec, are capable of detecting single 20-keV photons with a spatial resolution of ~0.2 mm. The detectors consist of an x-ray to optical conversion phosphor, a multistage image intensifier, and a CCD image readout.

I. INTRODUCTION

The relatively new field of x-ray astronomy has led to the discovery of entirely new classes of celestial objects and has provided us with new insights into the final evolutionary stages of stars and the origin of high-energy processes in the galaxy.

*Dr. Rygg died on March 14, 1975.

Among the more interesting phenomena are the recently discovered gamma-ray bursts (Ref. 1). These infrequent, transient events produce intense fluxes of x-rays and gamma-rays relative to the background. Position data is poor, although the sources appear to have an isotropic distribution. Although many theories for the bursts have been proposed (Ref. 2), it appears that a satisfactory explanation may have to await accurate measurement of their positions so that they may be identified with a particular type of optical or radio object. Such a measurement presents a unique experimental problem. Because of their apparently random occurrence in space and their brief duration – as short as 0.1 sec – it is necessary to use a wide-field detector. Since observable bursts occur infrequently and apparently randomly in time, the detector must be in continuous operation above the atmosphere for long periods.

The instrument we have developed for locating discrete, brief bursts of x-rays and gamma-rays is termed a "shadowgraph" and combines the features of wide field, high efficiency, and good angular resolution. Image readout by a CCD confers an advantageous combination of simplicity, integrating capability, and energy discrimination of the x-ray spatial detector compared with other position-sensitive x-ray detectors. The x-ray system has thus far been tested only by photographic means rather than by CCD readout. Since CCD technology is expected to improve greatly before the first operational shadowgraph, this paper will stress the experimental techniques and capabilities of the shadowgraph and the specifications of CCDs optimized for this application.

II. PRINCIPLE OF OPERATION

The shadowgraph is composed of a large dome-like occulting shadow mask and a number of x-ray imaging detectors located inside to detect an x-ray shadow cast through any part of the shadow mask (see Figure 1). A typical mask is made from photoetched 0.5-mm-thick tungsten plate. This thickness would provide adequate opacity for x-rays with energies up to 150 keV. The solid angle subtended by the mask at the detectors determines the field of view of the instrument, which could, conceivably, cover 4π steradians.

Since it is assumed that the brief bursts arrive from a point source at a great distance (Ref. 1), the parallel incident x-ray beam would produce a sharp shadow of the coded mask on the face of an x-ray image detector. The x-ray

shadow projection angle is uniquely determined simply by finding the area on the mask which produced the shadow. The source direction is then derived from this shadow projection angle and the orientation of the spacecraft.

The angular resolution of the shadowgraph is $\Delta\theta \approx \Delta x/d$, where Δx is the spatial uncertainty of the image position and d is the distance between the image plane and the appropriate shadow mask section. There are several components which enter into Δx; among the most important are: (1) x-ray source photon statistics and background events, (2) flexing and thermal distortion of the shadow mask and image detector image system, and (3) uncertainty in the location of individual x-ray photon events. It is estimated that for a weak burst, with ~400 x-ray photons over a 100-cm^2 detector area, the value for Δx will be of the order ~1 mm. For a small Explorer-type satellite, an average value for d is ~70 cm, yielding a location uncertainty of $\Delta\theta \approx 1$ mm/70 cm = 5 arc minutes. Spacecraft motion during observation, and attitude uncertainty will increase the location error somewhat.

The uncertainty due to photon statistics and background events, Δx_1, has been examined in detail, both analytically and through computer simulations. Consider N_s photons incident on a shadow mask with a transmission factor r (ratio of open area to total area) and a characteristic pattern cell dimension ℓ. Also assume that there are N_b background events randomly spaced over the image detector area and that it is required to locate the pattern with a statistical uncertainty of n_σ standard deviations. Then

$$\Delta x_1 \approx \frac{n_\sigma^2 \ell (N_s + N_b)}{r N_s^2} \qquad (1)$$

Figure 2 shows the results of a simulation of x-ray images from various fluxes of signal photons from a point source incident on the shadow mask pattern, with r = 0.44. A portion of the pattern is shown at the top of the figure. The amount of random background or noise photons was also varied, being equal to 1/2, 1/5, or 1/10 of the number of signal photons, as indicated in the figure. A computer program was used to find the optimum fit between the total mask pattern and the discrete photon image pattern by shifting the image in small steps over the larger mask pattern and finding the minimum photon coverage.

Assuming that the image area is 10 cm X 10 cm, the optimized fit from the computer routine for the case of 200 signal photons and 100 noise photons was less than 0.6 mm, while the value obtained from Equation (1) is ~0.5 mm for a 2 σ error. Note that at this low signal level, the mask pattern is not visually recognizable. This demonstrates that relatively little information is required to ascertain the location of the source by this technique, since the image detected is a portion of a known pattern. Naturally, it would be impossible to reconstruct a meaningful image from only 200 photon locations.

Since the locating accuracy for weak x-ray or gamma-ray bursts is dependent mainly upon photon statistics, it is desirable to obtain the highest ratio of signal photons to background photons in a particular energy range. Among the considerations that determine the optimum energy range are: (1) the spectrum expected from the source object, (2) the spectra of various components of the background such as the diffuse x-ray background and secondary x-ray and gamma-ray fluxes produced by charged-particle interactions; and (3) the efficiency of the shadowgraph mask and image detector combination. A rather detailed analysis of the combined spectral effects yields an optimum x-ray energy range of ~20 keV to ~100 keV in which to make observations of gamma-ray bursts.

III. IMAGING DETECTORS

The imaging detector is the most critical component for the shadowgraph and other x-ray multiplex methods such as the scatter-hole or Dicke camera (Refs. 3, 4). For this application, the essential characteristics are: (1) good spatial resolution irrespective of angle of incidence of the x-ray photon, (2) high detection efficiency over the energy range of interest, (3) large sensitive area, and (4) capability for observing a large range of burst intensities.

After studying several alternatives, the phosphor-image intensifier system (Figure 3) was chosen as the most suitable wide-field image detector for the energy region up to 100 keV. In this system, the x-ray photon is first converted into optical photons in a relatively thick (0.5 to 1.0 mm) phosphor. Present phosphors under study include rare-earth phosphors and cesium iodide. The energy conversion efficiency of these phosphors is in the range from 5% to 15%, so that a 20-keV photon will result in ~10^3 photons in the range 4000 Å to 5000 Å. The optical signal having a spot size of ~1 mm^2 is intensified and

demagnified by a multistage, electrostatically focused image intensifier. The image is then transferred by a lens onto a CCD for image readout.

Overall image reduction is from 80 mm X 80 mm at the x-ray phosphor to about 6 mm X 6 mm at the CCD. Linear spatial resolution at the x-ray phosphor of 0.5 mm thus requires a 160 X 160 element CCD array of area about 6 mm square. Grey level encoding of 4 bits would be sufficient to provide coarse energy resolution for each detected x-ray. The energy information would be used in the data analysis to eliminate sources of background such as dark current, high-energy gamma-ray Compton events, and charged particles. It is anticipated that the x-ray image integration time will be of the order of 1 sec, which may require operating the CCDs at temperatures below 0° C. Such temperatures would also reduce the dark current of the image intensifiers. The total image data expected from a single x-ray burst is several megabits. Present CCD technology requires that this data be stored in a nonvolatile, onboard digital storage device (possibly a CCD memory) for later transmission to a ground station.

The pictures in Figure 4 are output images of an experimental setup in our laboratory to study properties of intensifiers and x-ray converter phosphors. Two three-stage image intensifiers (Varo models 8583 and 8605) were coupled by an f/1.4 lens. A 0.5-mm-thick rare-earth phosphor was placed directly on the fiber optic input of the first intensifier (25-mm diameter), and the output of the second intensifier was photographed on Tri-X film with a 35-mm single-lens reflex camera. Figure 4 shows three photographs obtained with this system: two with weak radioactive sources present and one with background only. Individual x-ray photons can easily be observed from Co^{57} (122 keV) and Am^{241} (60 keV). All three photographs were obtained under the same conditions, outlined in Figure 4. The centroid of the brighter x-ray images can be determined to within ~0.2 mm.

It appears that the imaging requirements for an x-ray shadowgraph in terms of array size, resolution, and dynamic range can be met by current CCD technology. For a space-borne experiment, a CCD image readout offers great advantages of simplicity, small size, low power, low weight, and image positional stability compared to any conventional TV tubes. Areas of potential concern include long-term gain stability, image degradation during integration, and reliability.

REFERENCES

1. Klebesadel, R. W.; Strong, I. B.; and Olson, R. A.: Astrophys. J.; Vol. 182, p. L85 (1973).

2. Ruderman, M. A.: Proceedings Seventh Texas Symposium on Relativistic Astrophysics, New York Academy of Sciences (to be published, 1975).

3. Dicke, R. H.: Astrophys. J., Vol. 153, p. L101 (1968).

4. Ables, I. G.: Proc. Astron. Soc. Australia, #4, p. 1 (1968).

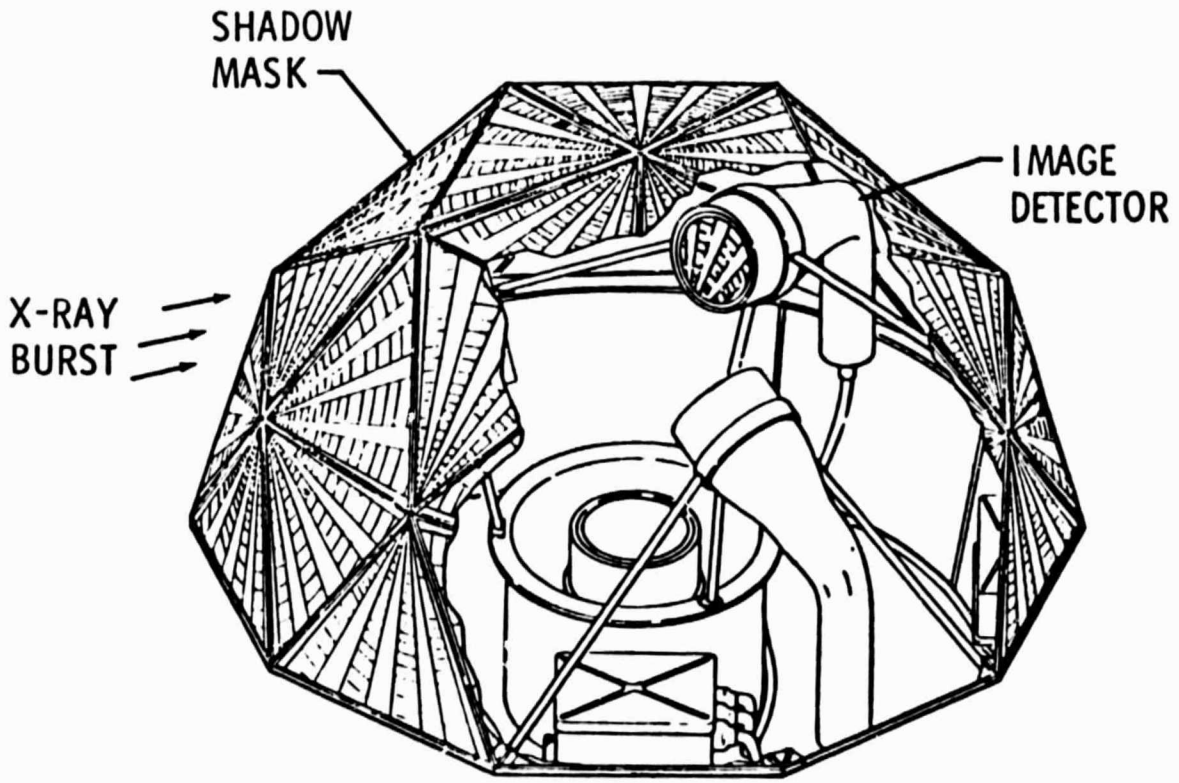

Figure 1. Shadowgraph experiment components (As shown, an x-ray burst incident from the left would cast an x-ray shadow on the forward-facing image detector.)

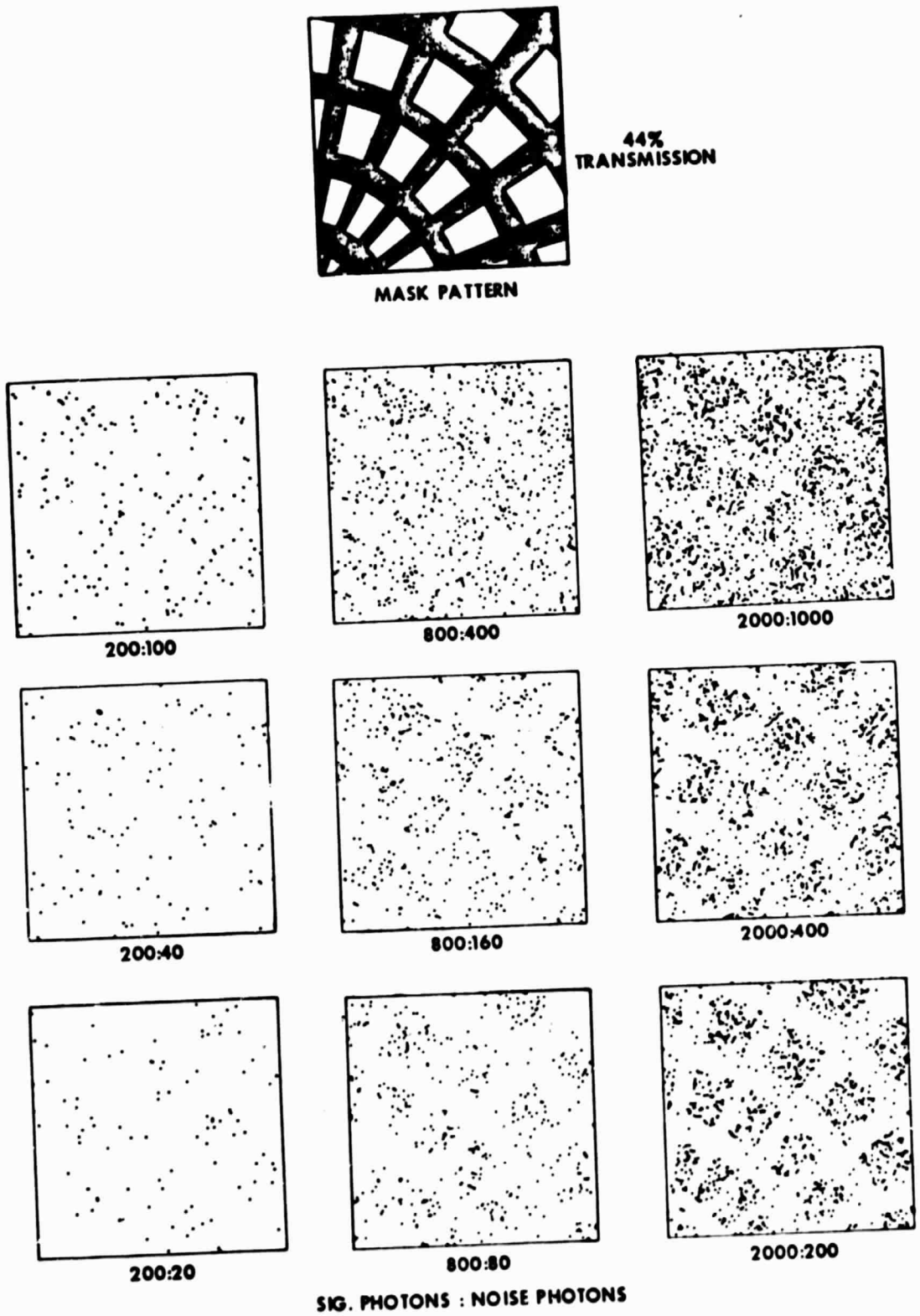

Figure 2. Simulated shadowgraph images showing effects of signal and noise photon statistics (The incident source photons are transmitted through the open areas of the mask pattern at the top, which represents a portion of the large shadow mask.)

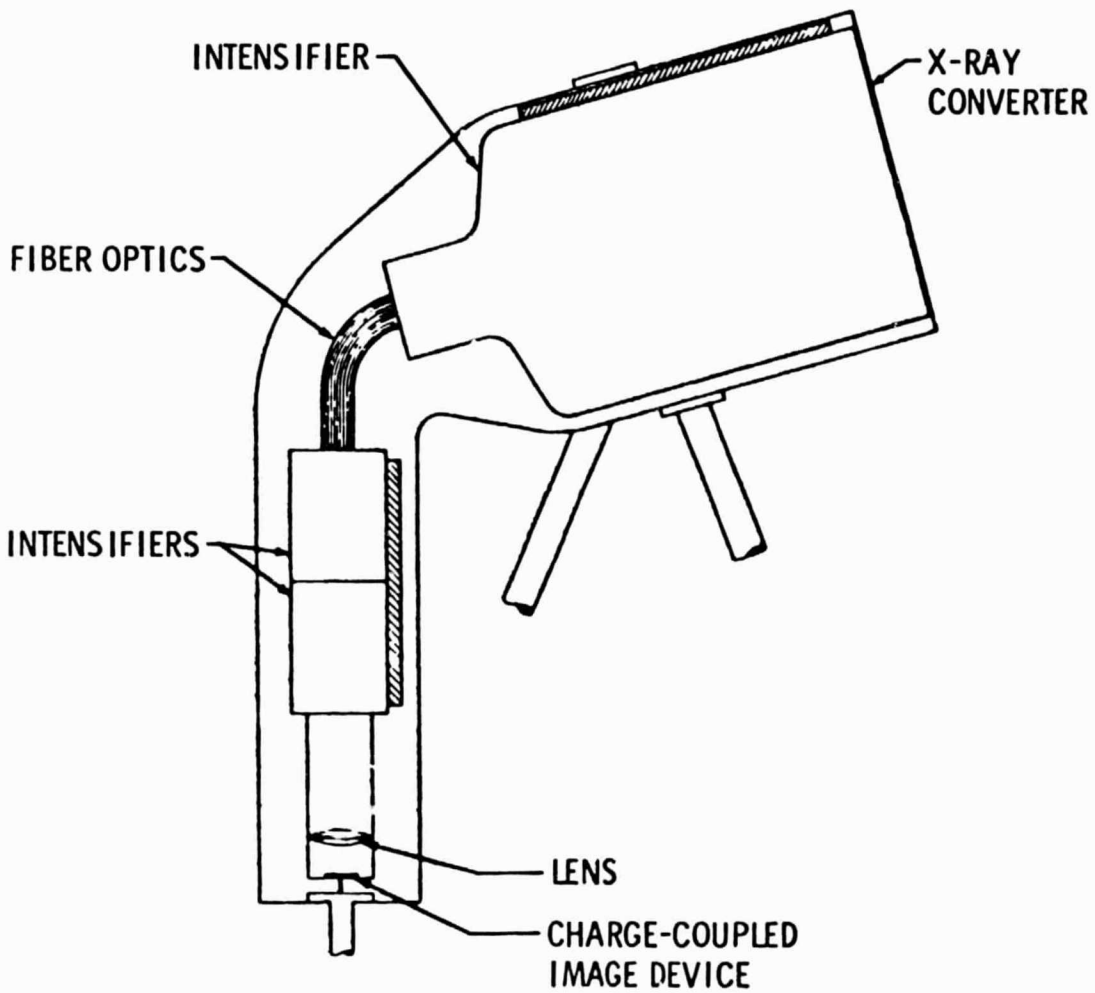

Figure 3. X-ray image detector schematic (The first-stage intensifier is an 80-mm/20-mm zoom-type intensifier. Additional stages are required to produce a suitable intensity for the CCD. It may be possible to improve the overall efficiency by coupling the CCD with fiber optics or even by locating the CCD internally in the last intensifier stage.)

X-RAY TEST PICTURES

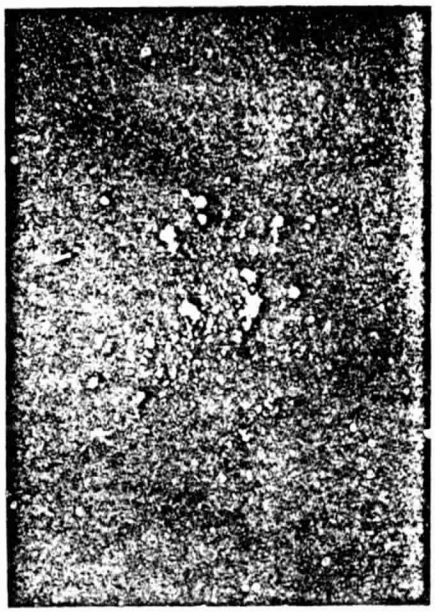

EXPOSURE: 0.125 sec
PHOSPHOR: RARE EARTH
THICKNESS: 0.5 mm
TEMP.: 20^0 C
GAIN: $\sim 10^6$
SCALE: ⊢ 1 mm

Am^{241} 60 KeV

Co^{57} 122 KeV

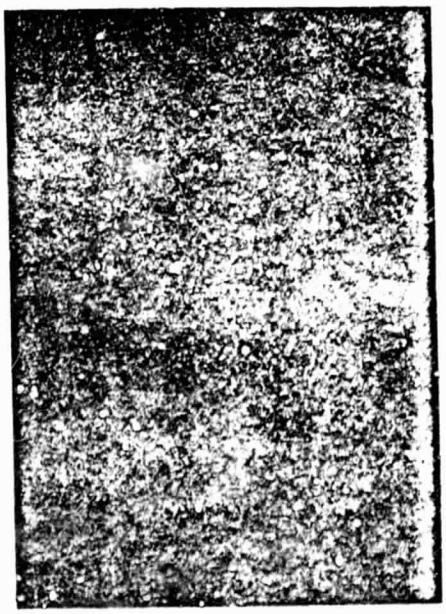

BACKGROUND

Figure 4. X-ray test photographs of a rare-earth phosphor/multi-stage intensifier system (Single x-ray photons at 60 keV and 122 keV are visible. Intensifier input diameter is 25 mm. X-ray spot size is ~0.5 mm. The centroid of each spot can be determined to less than 0.2 mm.)